

THESIS FOR THE DEGREE OF DOCTOR OF PHILOSOPHY

The pore geometry of pharmaceutical coatings: statistical  
modelling, characterization methods and transport prediction

SANDRA BARMAN



**CHALMERS**

*Division of applied mathematics and statistics*  
*Department of mathematical sciences*  
CHALMERS UNIVERSITY OF TECHNOLOGY  
AND THE UNIVERSITY OF GOTHENBURG  
Gothenburg, Sweden 2020

The pore geometry of pharmaceutical coatings: statistical modelling, characterization methods  
and transport prediction  
SANDRA BARMAN

ISBN 978-91-7905-273-7

Doktorsavhandlingar vid Chalmers tekniska högskola, Ny serie nr 4740

ISSN 0346-718X

© Sandra Barman, 2020.

Department of Mathematical Sciences  
Chalmers University of Technology  
and the University of Gothenburg  
SE-412 96 Göteborg  
Sweden  
Telephone + 46 (0)31-772 10 00

Printed by Chalmers Reproservice, Gothenburg, Sweden, 2020.

Some images that are in color in the electronic version of the thesis were printed in greyscale.

# The pore geometry of pharmaceutical coatings: statistical modelling, characterization methods and transport prediction

Sandra Barman

*Department of Mathematical Sciences  
Chalmers University of Technology and the University of Gothenburg*

## Abstract

This thesis contains new methods for bridging the gap between the pore geometry of porous materials and experimentally measured functional properties. The focus has been on diffusive transport in pharmaceutical coatings used in controlled drug delivery systems, but the methods are general and can be applied to other porous materials and functional properties. Relatively large datasets are needed to train realistic models connecting the pore geometry and diffusive transport properties of porous materials. 3-D statistical pore models based on microscopy images of the coating material were in this thesis used to generate large sets of pore structures, in which diffusive transport was computed numerically. Characterization measures capturing important features of the pore geometry were developed and used as predictors of diffusive transport rates in multiplicative regression models. The characterization measures have been implemented in a freely available software, MIST.

In Paper I, a Gaussian random field based pore model was developed and fitted to microscopy images of the coating material. Due to the large size of the data, the model was formulated using a Gaussian Markov random field approximation, which allows for efficient inference. A new method for solving linear equations with Kronecker matrices which reduced the complexity of the model fitting algorithm considerably was developed. The pore model was found to fit the microscopy images well. In Paper II, characterization measures that have been shown to provide good regression models for diffusive transport rates were developed further and implemented. Multiplicative regression models were fitted to pore structures from the model from Paper I, and the new methods were shown to give improved results. In Papers III and V characterization measures that capture a type of bottleneck effect which was observed in another set of microscopy images of the coating material (Papers III and IV), but which is not captured by existing methods, were invented. Pore structures with this type of bottleneck were generated using 3-D statistical pore models, and the new type of bottleneck was found to be an important determinant of diffusive transport rates when the regression models were fitted to simple pore structures (Paper V).

**Keywords:** Porous materials, controlled drug release, statistical pore model, Gaussian random fields, Gaussian Markov random fields, efficient inference, pore geometry characterization, bottleneck effects, diffusive transport modelling.



## Preface

This thesis is based on the work described in the following appended papers:

**Paper I.** A statistical model for imaged microstructures of porous polymer films. **S. Barman** and D. Bolin. *Journal of Microscopy*, 269(3): 247–258, 2018.

**Paper II.** Prediction of diffusive transport through polymer films from characteristics of the pore geometry. **S. Barman**, H. Rootzén and D. Bolin. *AIChE Journal*, 65(1), 446–457, 2019.

**Paper III.** New Characterization Measures of Pore Shape and Connectivity Applied to Coatings used for Controlled Drug Release. **S. Barman**, C. Fager, M. Röding, N. Lorén, C. von Corswant, E. Olsson, D. Bolin and H. Rootzén. Manuscript.

**Paper IV.** 3D High Spatial Resolution Visualisation and Quantification of Interconnectivity in Polymer Films. C. Fager, **S. Barman**, M. Röding, A. Olsson, N. Lorén, C. von Corswant, D. Bolin, H. Rootzén and E. Olsson. Manuscript.

**Paper V.** New measures of bottleneck effects in pore geometries evaluated through prediction of diffusive transport. **S. Barman**, H. Rootzén and D. Bolin. Manuscript.

The thesis also contains a description of the following software:

**Software MIST.** MIST – A program package for visualization and characterization of 3D geometries. 2019. **S. Barman**, D. Bolin, C. Fager, T. Gebäck, N. Lorén, E. Olsson, H. Rootzén, and A. Särkkä.

My contributions to the work presented in the appended papers and to the development of the software MIST:

**Paper I.** Participated in model selection and development of the inference method and goodness of fit-assessment. Discovered the method for solving linear equations using the Kronecker structure of the matrix. Implemented the methods, analyzed the results, drafted and edited the manuscript.

**Paper II.** Participated in the development of the method, selected the characterization methods, implemented the methods and carried out the simulation study, analyzed the results, drafted and edited the manuscript.

**Paper III.** Invented the new characterization methods, implemented the characterization methods, analyzed the results, drafted and edited the manuscript.

**Paper IV.** Participated in the development of the characterization and visualization methods based on geodesic paths, implemented those methods, participated in the analysis of the results, drafted parts of the manuscript, edited the manuscript.

**Paper V.** Participated in the development of the methods, created the pore models, implemented the methods and carried out the simulation study, analyzed the results, drafted and edited the manuscript.

**Software MIST.** Drafted a suggestion for what the software would include, led the collaboration with BOID – Project Design Studio and Chalmers Industriteknik in the development of the user interface, implemented the characterization methods based on geodesic paths, created the videos and document showing how to use the software.

## Acknowledgements

I greatly appreciate the funding from the Swedish Foundation for Strategic Research to the project “Material structures seen through microscopes and spatial statistics” which this thesis is a part of. I want to thank my supervisor Holger Rootzén. Your inspiring guidance and support has been invaluable. I want to thank David Bolin, my co-supervisor, for always giving such good feedback and advice. I also want to thank Aila Särkkä, my examiner, in particular for your feedback and role in guiding the project. Together, you—Holger, David and Aila—have made it such a nice project to be part of.

I also want to thank everyone involved in the project, especially Christian von Corswant, Cecilia Fager, Mats Josefsson, Niklas Lorén, Anna Olsson, Eva Olsson and Magnus Röding for your parts in the making of this thesis. I am grateful to AstraZeneca for supplying the datasets, Catherine Boissier, MariaGrazia Marucci and Henrike Häbel for providing the data that was used in Paper I, everyone involved in producing the datasets used in Papers III and IV and Tobias Gebäck for providing the software Gesualdo. I also appreciate the feedback given within the Chalmers center SuMo Biomaterials, and the feedback given in the recent workshops within the COSIMA project led by Tobias. I am also happy to have been part of developing the software MIST, with help and guidance from Aila, Holger, David and Tobias. I would especially like to thank Aila for initiating the project, and Tobias for being part of the developing process and helping me with the difficult parts of the C++-programming. To Cecilia, thank you for being both a friend and a colleague, for giving a valuable perspective from outside of mathematics, and for making it so much fun to work together on our common papers.

I am also grateful to all colleagues at the mathematical department for making this such a friendly place to work. I feel like I never want to leave here. Finally, I want to thank my family and friends, and especially my mother, for always being there.



# Contents

<b>1</b>	<b>Introductory summary</b>	<b>1</b>
<b>2</b>	<b>Polymer blends used as coatings in controlled drug release systems</b>	<b>5</b>
2.1	Data collection: microscopy techniques and image analysis . . . . .	6
<b>3</b>	<b>Spatial statistics</b>	<b>7</b>
3.1	Models . . . . .	8
3.1.1	Random fields . . . . .	8
3.1.2	Approximations of Gaussian fields: Gaussian Markov random fields . . .	9
3.1.3	The SPDE connection between Matérn random fields and discretely indexed (Gaussian) Markov random fields . . . . .	11
3.1.4	Hierarchical modelling . . . . .	13
3.2	Inference . . . . .	14
3.2.1	Markov chain Monte Carlo methods . . . . .	15
3.2.2	Goodness of fit . . . . .	18
<b>4</b>	<b>Connecting pore geometry properties to diffusive transport</b>	<b>21</b>
4.1	Diffusion . . . . .	21
4.1.1	Bounds . . . . .	23
4.2	Important pore geometry factors . . . . .	23
4.2.1	Simple sectioned model for diffusion in a single pore . . . . .	25
4.3	Pore geometry measures . . . . .	29
4.3.1	Path lengths . . . . .	30
4.3.2	Bottleneck effects . . . . .	30
4.4	Multiplicative regression models for predicting diffusion . . . . .	31
<b>5</b>	<b>Summary of appended papers</b>	<b>33</b>
5.1	Paper I . . . . .	33
5.2	Paper II . . . . .	36
5.3	Paper III . . . . .	38
5.4	Paper IV . . . . .	40
5.5	Paper V . . . . .	41
<b>6</b>	<b>MIST, a program package for visualization and characterization of 3-D geometries</b>	<b>43</b>
	<b>References</b>	<b>45</b>



---

# 1 Introductory summary

Porous materials have a wide range of applications, such as functional material design, e.g. metallic foams with tailored acoustic, thermal or mechanical properties (Lefebvre et al., 2008); electrochemical engineering, e.g. fuel cell optimization (Weber et al., 2014); biomedical engineering, e.g. scaffolds for tissue engineering (Moore, 2004); and pharmaceutical engineering, in the case of controlled drug release from pharmaceutical dosage forms (Siepmann et al., 2012, Ch. 9). Common for all of these applications is the demand for porous materials with strictly controlled functional properties. This thesis contains work related to a polymer material that is used as a coating of pellets in controlled drug release systems. The dosage forms containing coated pellets are only effective controlled release systems if the drug transport rate through the coatings are predictable and can be calibrated with high precision (Siepmann et al., 2012).

The drug diffuses from the core of the pellets through the pore structure of leached coatings, and the diffusive transport rate is determined by the pore geometry of the coating. As an aid in the development of improved coatings with precise transport rates, it is therefore important to be able to connect the pore geometry of the coatings to observed transport rates. This thesis contains general methods for making this connection. The methods were developed based on datasets obtained from microscopy images of the coating material, but the methods are applicable to other types of porous materials as well, especially materials with pore volume fractions similar to the coating material studied here. The methods are also applicable to other functional properties, in particular thermal and electrical conductivity properties since the governing equations for these are mathematically equivalent to the diffusion equation (Torquato, 1991), see e.g. Berg (2012); Harris and Lu (2013) and Holzer et al. (2013b).

To construct realistic models of diffusive transport, large datasets are needed to train the models, and accurate representations of the pore geometry of the studied material are also needed. Advances in microscopy techniques in recent years have made it possible to obtain high-resolution 3-D images of porous materials (Heng et al., 2007; James et al., 2012; Anovitz and Cole, 2015). Manufacturing, processing and imaging the material is however both time-consuming and costly, as is performing diffusion experiments. Virtual experiments provide valuable complements to real experiments.

In this thesis, 3-D statistical pore models were formulated to fit microscopy images of the coating material (Paper I) and to capture important features of the pore geometry obtained from the images (Paper V). Virtual experiments were performed in pore structures generated from the pore models by computing diffusion numerically using the software Gesualdo (Gebäck and Heintz, 2014). The virtual diffusion experiments were then used to fit multiplicative regression models connecting the pore geometry to diffusive transport rates, for large sets of pore structures

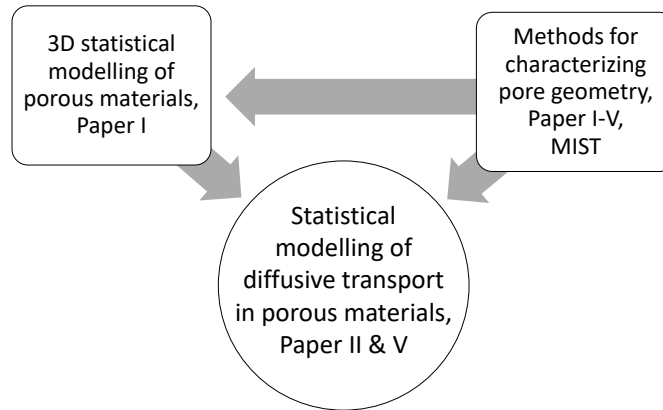


Figure 1: Overview of this thesis.

generated from the pore models (Papers II, V). Characterization measures that capture features of the pore geometry that are important determinants of diffusive transport were developed (Papers II, III, V) and used as predictors in the multiplicative regression models, following Stenzel et al. (2016). The limiting factor in this virtual experimental setup was the numerical diffusion simulation. A much larger set of pore structures could nevertheless be used in the virtual experimental setup compared to what would have been reasonable for real experiments.

The main components of this virtual experimental setup that are addressed in this thesis are shown in Figure 1. Other important components, such as microscopy imaging, image analysis and numerical approximations of diffusive transport are addressed to some extent in the appended papers, but are not the focus of the thesis. Now a short summary of the contents of the appended papers:

A 3-D statistical pore model was in Paper I fitted to confocal laser scanning microscopy images of the coating material, produced in connection with the work presented in Häbel et al. (2017). The model was based on the family of oscillating Matérn Gaussian random fields from Lindgren et al. (2011). A separable covariance was used to model the anisotropy in the data, and the model was reformulated as a Gaussian Markov random field to allow for efficient inference. A new method for solving linear equations involving Kronecker matrices, which has not been used in this context before, was used to reduce the computational cost of the model fitting algorithm further, allowing the model to be fitted to larger subsets of the microscopy images. The pore model was found to fit the microscopy images well.

Characterization methods that have in Brémond et al. (1994); Stenzel et al. (2016, 2017) been shown to be good predictors of diffusive transport (or the equivalent electrical conductivity property) were implemented for Paper II, and were used as predictors of diffusive transport rates in multiplicative regression models computed for pore structures generated from the pore model from Paper I. The characterization methods were related to path length (geodesic tortuosity) and bottleneck effects caused by variations in pore size (constrictivity), which have long been thought to be important determinants of diffusive transport (Petersen, 1958; Currie, 1960). New predictors were in Paper II shown to give improved multiplicative regression models, especially

---

a new version of the tortuosity factor compared to the tortuosity factor used in Stenzel et al. (2016, 2017), but the constrictivity was not a good predictor for the dataset used in the paper.

A type of bottleneck effect caused by many paths converging in the same pore, that is not captured by the existing bottleneck measures was observed in Papers III and IV in the pore geometry obtained from a set of focused ion beam scanning electron microscopy images of the coating material from Fager et al. (2020). A new characterization measure, termed the geodesic channel-strength, capturing this type of bottleneck effect was introduced in Paper III. The effect this type of bottleneck has on diffusive transport rates was investigated in Paper V, again using multiplicative regression models. The geodesic channel-strength and additional new characterization measures, designed to capture other aspects of the bottleneck effect, were used as predictors in the regression models, as were some of the predictors from Paper II.

An argument for fixing the exponent of the geodesic tortuosity in the regression models was presented in Paper II, based on a simple model of diffusive transport in pore structures consisting of separate, tortuous tubes. The effects of fixing the exponent were investigated in both Paper II and Paper V. The geodesic channel-strength was in Paper V shown to be an important complement to the geodesic tortuosity when the exponent was fixed to its theoretical value. From the results from fixing the exponent, and also from comparing regression models with only the tortuosity as a predictor fitted to different datasets, it was concluded that the tortuosity explains a larger portion of the variability in transport rates than predicted by theory. This is probably caused by a highly correlation between the tortuosity and other factors such as the prevalence of dead ends and the bottleneck effects caused by many paths converging in the same pore. To create a realistic model of diffusive transport that fits many different types of pore structures, it is important to separate these effects into different characterization measures. Paper V is a first step in this direction.

A freely available software called MIST has been developed to make the characterization methods implemented and developed in this thesis easily available (Barman et al., 2019). The idea of the software is to make it easy to explore the results of the characterization visually. The type of analysis that can be performed using the software is exemplified in Papers III and IV. The software can be downloaded from the link provided in Section 6.

The rest of the thesis is structured as follows: In Chapter 2 some details about the coating material studied in the thesis, as well as information about the microscopy imaging methods and image analysis methods that were used to obtain the datasets presented in Papers I, III and IV. A background on the 3-D statistical model, model fitting algorithm, and goodness of fit-measures which are used in Paper I is given in Chapter 3. Chapter 4 contains information about diffusive transport, along with the main ideas underlying the characterization methods and multiplicative regression models developed to connect pore geometry to diffusive transport rates in Papers II–V. A detailed summary of the appended papers is given in Chapter 5, followed by a description of the software MIST. This is followed by the appended papers.



## 2 Polymer blends used as coatings in controlled drug release systems

Controlled drug release is an important research area within pharmaceutical science. It can among other things reduce the variability of performance and improve the drug effectiveness by targeting a specific part of the body, and can help keep the concentration of the drug from fluctuating too much (Siepmann et al., 2012, Ch. 2). Porous materials are frequently used for controlled release. The rate of release is highly influenced by the pore geometry of the material.

The ethyl-cellulose/hydroxypropyl-cellulose (EC/HPC) material studied in this thesis (Papers I, III, IV) is used to coat pellets, which have a core containing drug enclosed by a porous coating that controls drug release (see Figure 2). A wide range of release rates can be achieved by using a blend of two different polymers (Siepmann et al., 2008). The HPC is water soluble while the EC is not, and so the HPC will be leached out when the pellet is immersed in water, creating a porous structure through which the drug can be transported. The pore structure is determined by the polymers' molecular weights and by processing parameters such as the temperature and spraying rate used in the manufacturing (Marucci et al., 2009, 2013; Andersson et al., 2013). The main mass transport mechanism for transport above a critical weight ratio of 22% HPC—below which the HPC rich domains do not form a continuous phase—is diffusion (Marucci et al., 2009).

Previous work on these free films of the EC/HPC coating material can be found in Häbel et al. (2016) and Häbel et al. (2017), where the pore geometry was characterized and modelled using extracted pore skeletons, and in Gebäck et al. (2015), where mass transport in the pore

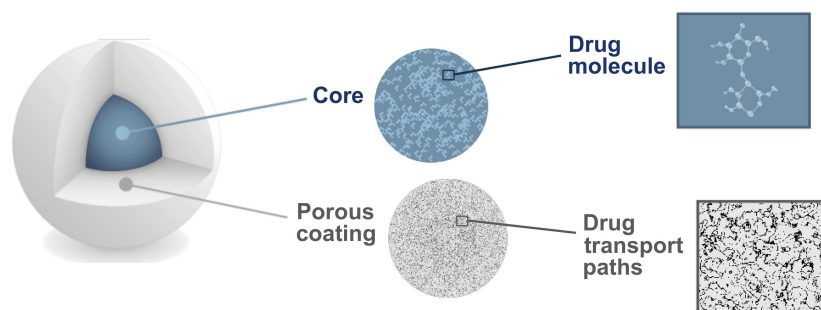


Figure 2: Illustration of a coated pellet with the core containing the drug and the EC/HPC polymer coating. The drug is transported along paths through the leached porous coating.

space of EC/HPC films was simulated numerically and compared to experimental results.

## 2.1 Data collection: microscopy techniques and image analysis

As mentioned above, advances in microscopy techniques have made it possible to obtain detailed images of the 3-D structure of porous materials. The microscopy data of the coating material used in this thesis were, as also mentioned above, obtained using confocal laser scanning microscopy (CLSM) (Paper I) and focused ion beam scanning electron microscopy (FIB-SEM) (Papers III, IV). The CLSM technique is non-destructive, i.e. it can be used to obtain a 3-D stack of images of a thick sample without slicing. Higher resolution images can be obtained using scanning electron microscopy, however images can only be obtained from the surface of the sample. The focused ion beam is used together with the electron microscope to mill thin slices, creating a 3-D stack of images of the sample. More details about the FIB-SEM technique can be found in Paper IV.

The microscopy images need to be processed to extract binary representations of the imaged pore geometry. A simple smoothing filter was applied to the CLSM images from Paper I. A more advanced image analysis algorithm was used on the same dataset in Häbel et al. (2017) to obtain a skeleton representation of the pore structure corresponding to the leached EC/HPC films. A self-learning algorithm was used to obtain the pore geometry representation of the FIB-SEM images of leached films from Papers III and IV.

### 3 Spatial statistics

Spatial statistics is used to model spatial and spatio-temporal statistical dependence structures, which enables statistical inference for complex spatial datasets. Spatial statistical methods and models have applications in various fields, such as image analysis (He et al., 2004), cosmology (Verde et al., 2000), geology (Foxall and Baddeley, 2002), ecology (Law et al., 2009), material science (Mecke and Stoyan, 2002), epidemiology and spatial econometrics (Gelfand et al., 2010). There are four main groups of spatial models: continuously indexed random fields, discretely indexed spatial processes, point processes and random sets. Whereas a realization  $X(\omega)$  of a random variable  $X$  is a real number, a realization  $\Phi(\omega)$  of a random field  $\Phi$  is a function

$$\Phi(\omega) : T \rightarrow D.$$

$T$  and  $D$  are usually Euclidean spaces, but they can also be more complex spaces, as when  $T$  represents a surface or a network. For discrete spatial processes,  $T$  is a countable set, e.g., a lattice (Gelfand et al., 2010). A realization of a point processes  $\Phi$  on  $\mathbb{R}^d$  consists of discrete points  $\Phi(\omega) = \{\mathbf{t}_1, \mathbf{t}_2, \dots\} \subset \mathbb{R}^d$  distributed in space. Point processes can be seen as a special type of random set model. A realization  $\Phi(\omega)$  of a random set  $\Phi$  is simply a subset of the domain  $T$ . Other types of random sets include Boolean models, which are obtained by centering simple sets on points in a point process, line and surface processes, and thresholded random fields (Chiu et al., 2013). Realizations of three of the four types of spatial models can be found in Figure 3.

Many models from spatial statistics have been used to model porous microstructures. Thresholded Gaussian random fields were among the first stochastic models used (Torquato, 2002, p. 295), and such models have been used to characterize the microstructure and its relation to macroscopic properties of porous media in Adler et al. (1990); Roberts and Teubner (1995); Mukherjee and Wang (2007). Examples of other types of models being used to make inference about properties of porous media can be found in (Yeong and Torquato, 1998; Blunt et al., 2002; Malek et al., 2014; Kim and Pitsch, 2009; Hermann and Elsner, 2014; Gaiselmann et al., 2014). The family of models that were used for the polymer coatings in Paper I were hierarchical models where the binarized microscopy data was modelled as a random set obtained by thresholding a Gaussian random field plus noise. For computational efficiency, the Gaussian fields were approximated by discretely indexed Gaussian Markov random fields. These kinds of models are described in more detail below. Pore structures generated from two random set-models based on point processes, where the points were connected to form a network, were also used in Paper V.

## 3.1 Models

### 3.1.1 Random fields

A random field can also be seen as a collection of random variables

$$\{\Phi_{\mathbf{t}} : \mathbf{t} \in T\},$$

indexed by the parameter space  $T$ . For most random fields, and for the fields we consider here,  $E = \mathbb{R}$ . A basic concept are the finite-dimensional distributions

$$f_{\mathbf{t}_1, \dots, \mathbf{t}_n}(u_1, \dots, u_n) = P(\Phi_{\mathbf{t}_1} \leq u_1, \dots, \Phi_{\mathbf{t}_n} \leq u_n).$$

By the Kolmogorov existence theorem, for any family  $\{f_{\mathbf{t}_1, \dots, \mathbf{t}_n}, \mathbf{t}_1, \dots, \mathbf{t}_n \in T, n \geq 1\}$  of functions that satisfy certain basic conditions that make them admissible as finite-dimensional distributions, there exists a random field with those finite-dimensional distributions.

A random field is said to be stationary if the joint distributions of vectors  $(\Phi_{\mathbf{t}_1 + \mathbf{t}_0}, \dots, \Phi_{\mathbf{t}_n + \mathbf{t}_0})$  do not depend on  $\mathbf{t}_0$ , i.e. if translating the field by  $\mathbf{t}_0$  does not change the finite-dimensional distributions, and it is isotropic if the finite-dimensional distributions do not change when the field is rotated.

The covariance function of  $\Phi$  is defined as

$$C(\mathbf{t}, \mathbf{s}) = Cov(\Phi_{\mathbf{t}}, \Phi_{\mathbf{s}}).$$

For stationary fields the covariance only depends on the difference  $\mathbf{t} - \mathbf{s}$ , and we can write the covariance  $C(\mathbf{t} - \mathbf{s})$ . Similarly, the covariance of an isotropic field can be written as  $C(|\mathbf{t} - \mathbf{s}|)$ , where  $|\cdot|$  gives the Euclidean distance of a vector. Covariance functions of random fields are necessarily positive semi-definite functions. A random field is Gaussian if all finite-dimensional distributions are multivariate Gaussian. Since multivariate Gaussian random variables are

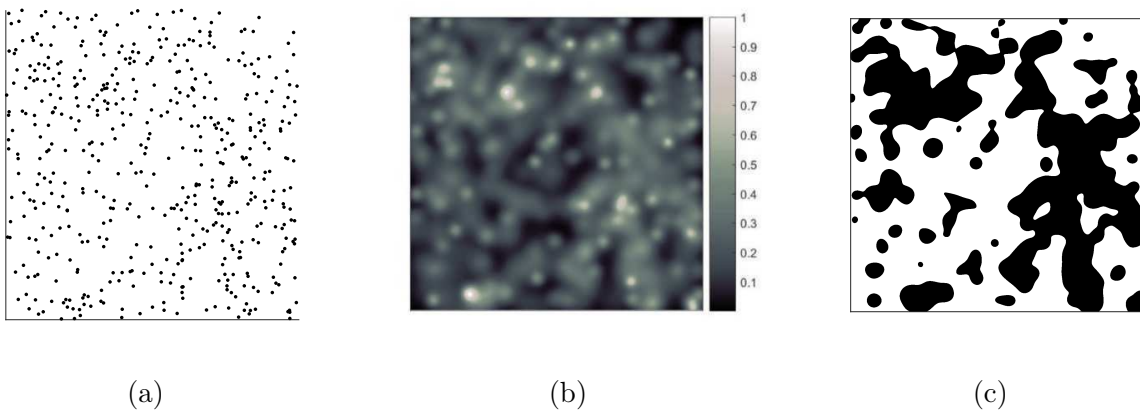


Figure 3: A realization of (a) a point process, (b) a discretely indexed random process, and (c) a random set. The realization in (b) is obtained by centering symmetric bivariate Gaussian densities, with random variance, on the points in (a). The realization in (c) is obtained by thresholding the realization in (b).

determined by their mean and covariance matrix, a Gaussian random field is also determined by its mean and covariance function. It follows from the Kolmogorov existence theorem that for any positive semi-definite function  $C$  there exists a Gaussian random field with  $C$  as its covariance function (Gelfand et al., 2010, Ch. 2).

These properties of Gaussian fields make them relatively easy to work with. Also, though it is in general difficult to prove results about properties of random fields such as a.s. continuity and exceedance probabilities, it is slightly easier for Gaussian fields, see Adler et al. (2013, Ch. 2.5–2.6).

Gaussian fields are the most commonly used random field (Gelfand et al., 2010, p. 149). Other types of random fields include transformations of Gaussian fields (Adler et al., 2013), which can be used e.g. to obtain heavier tails of the finite-dimensional distributions, and max-stable fields (Schlather, 2002), which are used to model extreme phenomena such as annual maximum rainfall. A classic random field application is kriging, which is used in, e.g., environmental studies and climatology (Cressie and Johannesson, 2008), where a field is interpolated from sparse observations. Kriging provides the best linear unbiased interpolation given that the covariance of the interpolated field is known (Gelfand et al., 2010, Ch. 3). Other applications involve excursion sets of random fields. These have been used to do inference in medical imaging, determining whether signals in PET-scan images are due to noise or related to brain areas important for specific tasks, and in astrophysics, where they have been used to understand the galactic topography using cosmic microwave background radiation (Adler, 2000).

### 3.1.2 Approximations of Gaussian fields: Gaussian Markov random fields

Assume that we want to generate a realization of a Gaussian field  $\Phi$  with zero mean and covariance function  $C$ , in some finite collection of points  $\{\mathbf{t}_1, \dots, \mathbf{t}_n\} \subset T$ . That is, we want to generate a realization of a Gaussian vector  $(\Phi_{\mathbf{t}_1}, \dots, \Phi_{\mathbf{t}_n}) \sim N(\mathbf{0}, \Sigma)$  with covariance matrix  $(\Sigma_{i,j})_{i,j=1}^n = (C(\mathbf{t}_i, \mathbf{t}_j))_{i,j=1}^n$ .

If we only consider the memory requirements for storing a full  $n \times n$  covariance matrix  $\Sigma$  on a laptop with 16GB RAM, the largest full matrix we can store in Matlab (MATLAB, 2017) is  $n = 45000$ . This is if the elements of the matrix are stored in double-precision, which provides 16 decimals of precision and requires 8 bytes storage for each element, and using the standard setting which only allows RAM and not virtual memory to be used when creating an array. If the points  $\{\mathbf{t}_1, \dots, \mathbf{t}_n\}$  are placed on a regular grid in  $\mathbb{R}^3$ , where  $m$  is the number of points in each dimension, the largest number for which the full covariance matrix of a Gaussian vector could be stored would be  $m = \sqrt[3]{n} = 35$ . These calculations do not even take into account memory requirements or computational complexity of covariance matrix operations. To generate a  $N(\mathbf{0}, \Sigma)$  random vector, we need to compute either the Cholesky factor of  $\Sigma$  or of the precision matrix  $\mathbf{Q} = \Sigma^{-1}$ , and calculating the Cholesky factor of a full  $n \times n$  matrix requires  $\mathcal{O}(n^3/3)$  operations. To deal with these computational issues, we need to find approximations of the Gaussian field that allow for efficient simulation and inference. Gaussian Markov random fields, which we will now define, provide one such approximation.

A discretely indexed spatial process  $\mathbf{w} = (w_i)_{i \in T}$  defines a function  $i \mapsto w_i, i \in T$ , where  $T$  is a countable parameter space, and  $w_i$  are random variables. It is often convenient to represent the parameter space as  $T = \{1, 2, \dots\}$ . Gaussian Markov random fields (GMRFs) are spatial

processes defined w.r.t. undirected finite graphs  $(T, E)$ ,  $T = \{1, \dots, n\}$ .  $E$  here contains the edges of the graph, so that  $i, j \in T$  are neighbours if  $(i, j) \in E$ . The graph  $(T, E)$  can e.g. represent a regular grid. The formal definition of a GMRF is the following:

**Definition 1.** A Gaussian vector  $\mathbf{w} \sim N(\mathbf{0}, \Sigma)$  is a GMRF w.r.t. the graph  $(T, E)$  if the precision matrix  $\mathbf{Q} = \Sigma^{-1}$  satisfies

$$Q_{i,j} = 0 \iff (i, j) \notin E, \forall i \neq j.$$

The sparsity (and graph structure) of a GMRF can be interpreted in terms of its dependence structure.  $\mathbf{w}_1$  and  $\mathbf{w}_2$  are conditionally independent given  $\mathbf{w}_0$ , denoted  $\mathbf{w}_1 \perp \mathbf{w}_2 \mid \mathbf{w}_0$ , where  $\mathbf{w}_0$ ,  $\mathbf{w}_1$ , and  $\mathbf{w}_2$  are sub-vectors of  $\mathbf{w}$ , if the conditional densities factor as  $\pi(\mathbf{w}_1, \mathbf{w}_2 \mid \mathbf{w}_0) = \pi(\mathbf{w}_1 \mid \mathbf{w}_0)\pi(\mathbf{w}_2 \mid \mathbf{w}_0)$ . For a non-singular multivariate Gaussian vector  $\mathbf{w}$ ,

$$Q_{i,j} = 0 \iff w_i \perp w_j \mid \mathbf{w}_{-ij},$$

where  $\mathbf{w}_{-ij} = (w)_{k \in T \setminus \{i,j\}}$ . The equivalence is similar to the equivalence of zero covariance and independent variables for Gaussian vectors. This result means that for a GMRF  $\mathbf{w}$ , two nodes in  $T$  which are not neighbours are conditionally independent when conditioned on the value of all other nodes. A GMRF with a specific sparsity structure can thus be constructed by controlling its conditional dependence structure.

GMRFs used in practice have sparse precision matrices (illustrated in Figure 4), even though sparsity is not a part of the definition. Sparsity of the precision matrix is very useful, since operations with sparse matrices can be much more efficient than with full matrices. For a sparse band-matrix with bandwidth  $p$ , the cost of a Cholesky factorization is only  $\mathcal{O}(n(p^2 + 3p))$ . The band-width of  $\mathbf{Q}$ , after a reordering of the nodes in  $T$ , could typically be around  $\sqrt{n}$ , in which case  $\mathcal{O}(n^2)$  operations are required (Rue and Held, 2005, Ch. 2.4.1). Additionally, the memory requirements for storing an  $n \times n$  sparse matrix with  $r$  non-zero diagonals are of order  $rn$ . With  $r = 5$ , the size of the largest grid in  $\mathbb{R}^3$ , for which we can store the precision matrix in Matlab (MATLAB, 2017) is around  $m^3$  for  $m = 370$ . These are large improvements compared to when using a full matrix. In Paper I, the Gaussian field was formulated in such a way that the feasible size of  $\mathbf{w}$  is increased further.

Imposing sparsity on  $\mathbf{Q}$  poses less restrictions on the Gaussian vector  $\mathbf{w}$  than imposing sparsity on  $\Sigma$ , as most covariances used for random fields can be well-approximated using sparse precision matrices (Rue and Tjelmeland, 2002). A downside is that finding a GMRF that approximates a specific covariance might be time-consuming. The SPDE connection of Lindgren et al. (2011) presented below solves this problem for the most commonly used family of covariance functions, the Matérn covariances.

GMRFs have many applications, see Rue and Held (2005, Ch. 1) for references to work in different areas of spatial statistics, as well as for work on time-series, longitudinal and survival data, graphical models and semi-parametric regression and splines. More details about the construction and properties of GMRFs can also be found in Rue and Held (2005).

A low-rank representation of a Gaussian field is another commonly used method of approximation. This method uses an expansion  $\Phi_{\mathbf{t}} = \sum_{i=1}^{\infty} \alpha_i \varphi_i(\mathbf{t})$  of the Gaussian field, where  $\alpha_i$  are independent  $N(0, 1)$ -variables, and  $\varphi_i$  are deterministic functions. An approximation of

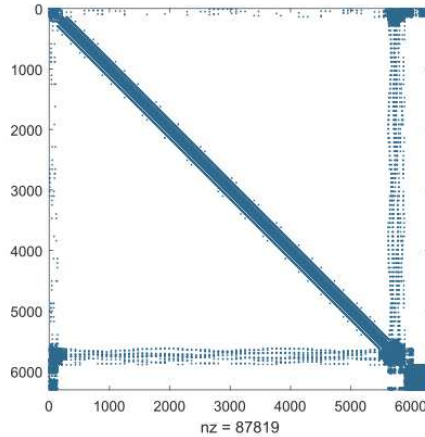


Figure 4: The sparsity pattern of a sparse precision matrix of a GMRF ( $\mathbf{Q}_{xy}$ , for dataset  $HPC30_1$ , of Paper I).

the Gaussian field is obtained by replacing the expansion by the sum  $\sum_{i=1}^N \alpha_i \varphi_i(\mathbf{t})$ . Different kinds of expansions are possible: the functions  $\{\varphi_i\}$  can be a Fourier basis, orthogonal polynomials, wavelets, and eigenvectors of the covariance matrix. Approximations are obtained by only keeping low-order terms in the expansion. The gain in computational efficiency depends on how many terms that are kept (Gelfand et al., 2010, Ch. 8). Approximations using the fast fourier transform (FFT) can be very efficient for random field simulation, as simulation requires  $\mathcal{O}(n \log(n))$  operations (Lang and Potthoff, 2011). A downside with using the FFT however is that it is difficult to extend the method beyond approximations on regular lattices, and knowledge about the covariance (or the related spectral density) is required (Lindgren et al., 2011). An advantage with using GMRF approximations is that likelihood-based inference in a hierarchical model setting can be implemented efficiently. GMRF approximations are also well suited for simulation from fields conditioned on data, in which case the precision matrix, not the covariance, is known explicitly. More details about this can be found in Chapter 3.2.1.

### 3.1.3 The SPDE connection between Matérn random fields and discretely indexed (Gaussian) Markov random fields

The Matérn family of covariance functions is the most popular family used for random fields (Gelfand et al., 2010, p. 24). The solution  $\Phi$  to the following stochastic partial differential equation (SPDE) was shown to be a Matérn Gaussian field in Whittle (1954, 1963):

$$(\kappa^2 - \Delta)^{(\nu+d/2)/2} \{\tau \Phi_{\mathbf{t}}\} = W_{\mathbf{t}}, \quad \mathbf{t} \in \mathbb{R}^d. \quad (1)$$

Here  $\kappa > 0$  and  $\nu > 0$  are the usual range and smoothness parameters of Matérn Gaussian fields,  $\tau > 0$  is a parameter that controls the variance,  $W$  is spatial Gaussian white noise, and  $\Delta$  is the Laplacian operator. Using the finite element method (Larsson and Thomée, 2003), the Matérn Gaussian field determined by the SPDE can be approximated by a GMRF,

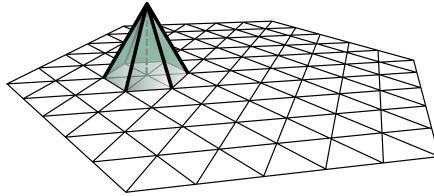


Figure 5: Triangulation of a domain  $T$ , showing one piece-wise linear basis function  $\varphi_i$ .

allowing efficient algorithms for inference for GMRFs to be applied. This link between Gaussian fields and GMRFs was presented in Lindgren et al. (2011), and has become widely used since. The finite element method is used to approximate solutions to deterministic partial differential equations (PDEs). The solution of a PDE is in a sense projected onto a low-dimensional function space  $V$  using a variational formulation. The space  $V$  consists of functions  $v$  which are linear combinations of basis functions  $\{\varphi_i\}$ , i.e.  $v(\mathbf{t}) = \sum_{i=1}^n \alpha_i \varphi_i(\mathbf{t})$ ,  $\mathbf{t} \in T$ , where  $T$  is the domain. The basis functions are commonly piece-wise linear or polynomial functions defined using a triangulation of the domain. An example of a basis function for piece-wise linear functions is shown in Figure 5. The finite element solution provides the weights  $\boldsymbol{\alpha} = (\alpha_1, \dots, \alpha_n)$  that define the approximate solution. In the stochastic setting of the SPDE, the weights, denoted  $\mathbf{w}$ , are stochastic and so the finite element approximation to the SPDE is a stochastic function  $v(\mathbf{t}) = \sum_{i=1}^n w_i \varphi_i(\mathbf{t})$ ,  $\mathbf{t} \in T$ . These stochastic coefficients determine a GMRF  $\mathbf{w} \sim N(\mathbf{0}, \mathbf{Q}^{-1})$  with a sparse precision matrix. The non-zero entries of  $\mathbf{Q}$  depend on the parameters of the SPDE and on the chosen basis functions  $\{\varphi_i\}$ . The triangulation of the domain makes the GMRF approximation flexible, as the nodes in the triangulation, which correspond to the entries of the GMRF, can be chosen to fit with observations of the field on irregularly spaced grids and irregular domains.

Formulating the Gaussian field using the SPDE (1) in this way has other advantages too. The SPDE formulation makes it straightforward to define random fields on manifolds, such as the sphere, making it well suitable e.g. for global climate modelling. The coefficients  $\kappa$  and  $\tau$  can be allowed to vary as functions of space, yielding non-stationary fields (Lindgren et al., 2011). Other types of non-stationary fields can also be obtained by changing the differential operators (Bolin and Lindgren, 2011), and non-Gaussian random fields can be obtained by letting the noise be non-Gaussian (Bolin, 2014; Wallin and Bolin, 2015). The finite element method to obtain (Gaussian) Markov random fields enables efficient inference also for these non-stationary and non-Gaussian fields. This is something which is not always easy for stationary Gaussian fields, and it is even harder in non-stationary and non-Gaussian cases.

The oscillating Matérn family of Gaussian fields, and corresponding GMRF approximations, that were used to define the model in Paper I (see Figure 6) are obtained from a complex reformulation of the SPDE (Lindgren et al., 2011). For this family, the covariance  $C(t)$  is negative for some  $t$ . There are not many families of covariance functions available with this property, although a few examples can be found in Chilès and Delfiner (2012, Ch. 2.5.1).

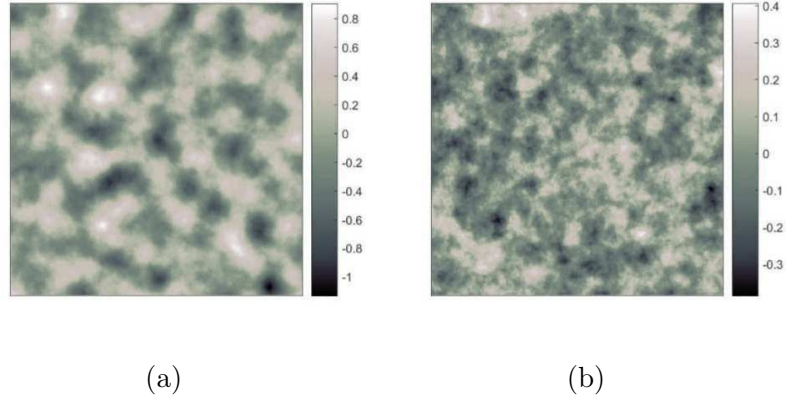


Figure 6: Realizations from two oscillating Matérn GMRFs, with (a) a high oscillation parameter and (b) zero oscillation parameter. Both GMRFs have the same parameter values  $\kappa^2$  and  $\tau$ .

### 3.1.4 Hierarchical modelling

Spatial datasets are often complex. There may be multiple sources of data, with complicated and unknown dependence structures and measurement error processes. Hierarchical modelling provides a flexible framework to deal with this kind of data. The basic idea of hierarchical modelling is to formulate models using conditional distributions. As a simple example, consider  $\mathbf{y} = (y_1, \dots, y_n)$  as the data, which we consider to be observations of an underlying GMRF  $\mathbf{w}$  with covariance  $\mathbf{Q}(\boldsymbol{\gamma})^{-1}$ , depending on parameters  $\boldsymbol{\gamma}$ , which is observed with independent measurement noise with variance  $\sigma^2$ . This model, which is illustrated in Figure 7, is formulated as

$$\begin{aligned} \mathbf{y}|\mathbf{w}, \boldsymbol{\gamma} &\sim N(\mathbf{w}, \sigma^2\mathbf{I}), \\ \mathbf{w}|\boldsymbol{\gamma} &\sim N(0, \mathbf{Q}(\boldsymbol{\gamma})^{-1}), \\ \boldsymbol{\gamma} &\sim \Pi. \end{aligned} \tag{2}$$

Here  $\mathbf{I} \in \mathbb{R}^{n \times n}$  is the identity matrix, and  $\Pi$  is some prior distribution. The underlying GMRF  $\mathbf{w}$  is called a latent field. The parameters  $\boldsymbol{\gamma}$ , called hyper-parameters, represent the highest level in the hierarchy. The model in Paper I was formulated similarly to (2), but with an additional step where the GMRF with added noise was thresholded to obtain the data.

In (2) the model framework is Bayesian, as we let the unknown hyper-parameters  $\boldsymbol{\gamma}$  be random variables. In a frequentist approach  $\boldsymbol{\gamma}$  would instead be considered to be fixed. It is important when formulating a model to consider the computational efficiency of algorithms for doing inference, as well as the plausibility of the model. The form of the posterior distribution

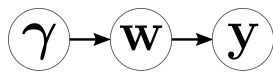


Figure 7: A graphical representation of model (2).

of the latent field, i.e., of  $\mathbf{w} \mid \mathbf{y}$ , is important for likelihood-based inference, see Chapter 3.2.1. Prior distributions for parameters can also be chosen to facilitate inference, for example by using conjugate priors. The influence of priors on inference should always be checked. For large datasets, the prior may not influence the results much at all, but this is important to check. The Gaussian assumptions should be verified as well.

The hierarchical model (2) can easily be extended to include more data sources by, e.g., letting the mean of  $\mathbf{y}$  depend on both  $\mathbf{w}$  and covariates. Popular hierarchical models include generalized linear models, where the dependence on covariates is linear, and generalized additive models, where the covariates are transformed by smooth functions (Fahrmeir and Lang, 2001; Christensen et al., 2006). See Gelfand et al. (2010, Ch. 7) for more information about hierarchical modelling in a spatial setting.

## 3.2 Inference

When doing inference we want to estimate the parameters of the model given data. In a Bayesian setting this involves evaluating the marginal posterior distributions of the parameters. Taking again model (2) as an example, the marginal posterior of  $\boldsymbol{\gamma}$  is obtained by integrating out the latent GMRF from the joint posterior density as

$$\pi(\boldsymbol{\gamma} \mid \mathbf{y}) = \int_{\mathbb{R}^n} \pi(\mathbf{w}, \boldsymbol{\gamma} \mid \mathbf{y}) d\mathbf{w},$$

where we use  $\pi(\cdot)$  to denote densities. This integral quickly becomes intractable. The conditional density  $\pi(\mathbf{w}, \boldsymbol{\gamma} \mid \mathbf{y})$  is a function of the precision matrix  $\mathbf{Q}(\boldsymbol{\gamma}) \in \mathbb{R}^{n \times n}$ , and just determining the proportionality constant to evaluate  $\pi(\mathbf{w}, \boldsymbol{\gamma} \mid \mathbf{y})$  can be very computationally demanding. A frequentist likelihood approach faces the same problems, since then the integral of the joint density  $\pi(\mathbf{y}, \mathbf{w}; \boldsymbol{\gamma})$  needs to be evaluated to integrate out  $\mathbf{w}$ . The marginal posterior distribution  $\mathbf{w} \mid \mathbf{y}$  of the latent field, which is of interest in many cases, can be just as difficult to obtain.

The best we can do is often to approximate the posterior distributions. Markov chain Monte Carlo (MCMC) algorithms are flexible methods for doing this, which is the kind of method that was used in Paper I. To find approximate maximum likelihood/maximum a posteriori estimates of the parameters the expectation maximization (EM) algorithm is another alternative (Dempster et al., 1977), along with other related iterative optimization methods (Lange, 1995). Integrated nested Laplace approximations, which is based on numerical integration, can be used when the latent GMRF is Gaussian (Rue et al., 2009). These methods, termed likelihood-based methods, can all be very computationally demanding. Minimum-contrast methods (Gaetan and Guyon, 2010), such as least-squares estimation that estimate model parameters by minimizing the least-square distance of e.g. empirical and model covariance functions, and pseudo-likelihood methods, that e.g. use only pairwise likelihoods, are less demanding, but are on the other hand less exact than likelihood-based methods. Both EM-algorithms and minimum-contrast methods have been used to fit thresholded Gaussian fields models, see Wilson and Nott (2001).

### 3.2.1 Markov chain Monte Carlo methods

Markov chain Monte Carlo (MCMC) methods have been used extensively in spatial statistics, both to do inference and for simulation. Many examples of applications can be found in (Brooks et al., 2011). MCMC methods are used when it is difficult to generate i.i.d. samples from the distribution of interest. Instead a Markov chain that has the distribution as its invariant distribution is used. An invariant distribution for a Markov chain  $(X_1, X_2, \dots)$  is a distribution such that if  $X_1$  has this marginal distribution, then all other elements of the Markov chain has this distribution as well.

The term Monte Carlo stands for numerical simulation of random processes (Brooks et al., 2011, p. 3). Monte Carlo integration is used to estimate expectations such as  $\mu = E[g(X)]$ . The estimator

$$\hat{\mu} = \frac{1}{n} \sum_{i=1}^n g(X_i), \quad (3)$$

where  $X_1, \dots, X_n$  are i.i.d., has the approximate distribution  $\hat{\mu} \approx N(\mu, \sigma^2/n)$  by the central limit theorem if  $\sigma^2 < \infty$ , where  $\sigma^2$  is the variance of  $g(X)$ . MCMC uses the fact that a similar central limit result holds when the i.i.d. sample is replaced by a stationary<sup>1</sup> Markov chain  $(X_1, X_2, \dots)$  which has the distribution of  $X$  as its invariant distribution (Brooks et al., 2011, p. 8) (under various conditions that can be found in Jones (2004)). The difference compared to ordinary Monte Carlo is that if the central limit theorem holds for the approximation  $\hat{\mu}$ , then the variance  $\sigma^2/n$  of the approximate normal distribution is given by

$$\sigma^2 = \text{Var}(g(X_i)) + 2 \sum_{k=1}^{\infty} \text{Cov}(g(X_i), g(X_{i+k})), \quad (4)$$

for any  $i$ . If  $g$  is vector valued, then the variance and covariances, termed auto-covariances, in (4) are matrices.

If  $X_1$  is generated from the invariant distribution, then the chain is stationary, in which case the estimator (3) is unbiased (Brooks et al., 2011, p. 21). But since MCMC is used when it is difficult to generate samples from the invariant distribution directly, the chain is often started using some approximation of the invariant distribution, and so the chain is not stationary and the estimator may be biased. There is however a law of large numbers that says that the estimator (3) converges with probability one to  $E[g(X)]$  as  $n \rightarrow \infty$ , for almost all starting values  $X_1$ , under conditions that the Markov chain is irreducible and recurrent (Johansen et al., 2007, Ch. 3.4). If the chain is Harris recurrent, then a central limit result holds as well regardless of the initial distribution of  $X_1$ , under the condition that it holds for one initial distribution. The conditions here on the Markov chain determines in a sense how well the set of values that can be attained under the invariant distribution is explored by the chain.<sup>2</sup> Additionally, the variance (4) of the stationary chain is the asymptotic variance of the chain, whether the chain

<sup>1</sup>A Markov chain is stationary if it is a stationary random process, i.e. if the distribution of  $(X_{k_1+k_0}, \dots, X_{k_n+k_0})$  does not depend on  $k_0$ , for all  $k_1, \dots, k_n \in \{1, 2, \dots\}, n > 0$ .

<sup>2</sup>Irreducibility implies that the full set of values attainable under the invariant distribution of the Markov chain can be explored, and the expected number of times a recurrent Markov chain visits any set with positive

is stationary or not (Brooks et al., 2011, p. 8).  $(X_n, X_{n+1}, \dots)$  can thus be seen to sample the invariant distribution when the Markov chain is irreducible and recurrent, regardless of the initial distribution, when  $n$  is large enough.

In practice, simulation of the Markov chain is often allowed to run long enough so that the run seems to be stationary, and the first part of the run which does not seem stationary, called the burn-in, is discarded. The remaining chain is assumed to be representative of the invariant distribution. This is a bit risky as the invariant distribution is often unknown, which makes it difficult to determine if the run is really representative. It could be that the Markov chain only explores a small part of the set of values attainable under the invariant distribution. Simple methods to handle this problem are to let the chain run for a long time after it has seemingly converged to stationarity, and to start several runs with different starting values  $X_1$ , although they do not provide any guarantees that the resulting runs are representative (Brooks et al., 2011, Ch. 1).

Different MCMC-algorithms use different methods to update the Markov chain, i.e. to generate  $X_{n+1} | X_n$ . Metropolis-Hastings updating is a common method which does not require the normalization constant of the density  $\pi_X$  of the invariant distribution to be known. We let  $h(x) = \alpha\pi_X(x)$ , for some  $\alpha > 0$ . The update works as follows:

1. Given the current state  $X_n$ , generate  $Y$  using the proposal density  $q(Y|X_n)$ .
2. Accept the proposed value  $Y$  with acceptance probability

$$p = \min \left( 1, \frac{h(Y)q(X_n|Y)}{h(X_n)q(Y|X_n)} \right).$$

If  $Y$  is accepted, go to step 3, otherwise go back to step 1.

3. Set  $X_{n+1} = Y$ .

Metropolis-Hastings algorithms are very versatile, since the proposal densities can be chosen in many different ways:  $q$  can be taken to be a close approximation to  $\pi_X$  from which it is easy to generate samples. It can also be unrelated to  $\pi_X$ , and only depend on the current state  $X_n$ , corresponding e.g. to a random walk around  $X_n$ .

Gibbs sampling is another common method to update the Markov chain. If  $X$  is a vector, a classic Gibbs sampler would generate each element of the vector  $X_{n+1}$  separately using its marginal conditional distribution (Brooks et al., 2011, Ch. 1.12). It is common to have a hierarchy of updating steps in a Gibbs sampler, where some of the marginal conditional distributions are updated using Metropolis-Hastings. This is the method that was used in Paper I.

An issue with MCMC algorithms is that they can be very time-consuming. The variance of the estimator (3), and thus the required number of iterations of the algorithm, can be decreased by reducing the auto-covariances of the chain. In Metropolis-Hastings updates, the acceptance probability can be optimized to obtain low auto-covariances. For Gibbs samplers,

---

probability under the invariant distribution is infinite. Harris recurrence is slightly stronger, and essentially means that the chain visits all sets that have positive probability under the invariant distribution infinitely many times, with probability one.

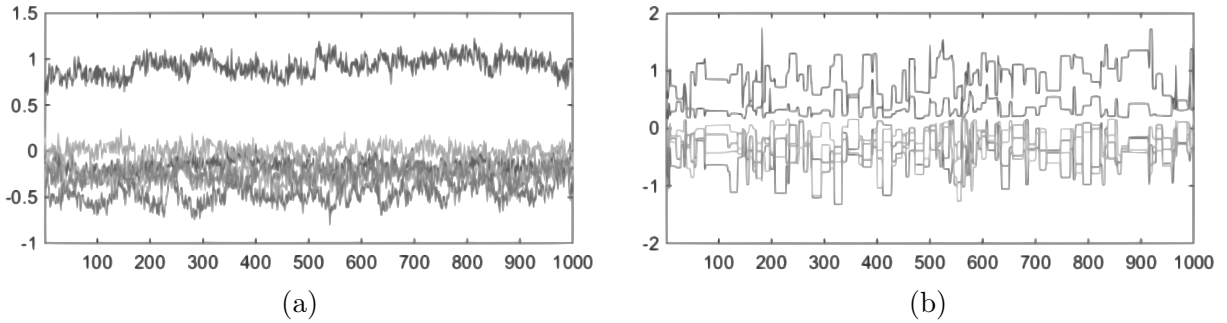


Figure 8: Trajectories of a Markov chain  $(X_1, \dots, X_{1000})$  with block Gibbs updating, showing (a) a block with high acceptance probability, and (b) a block with low acceptance probability. The trajectories are those of six elements of  $\mathbf{w}$  and  $\mathbf{s}$ , in (a) and (b) respectively, from part of an MCMC run for  $HPC30_1$  in Paper I.

blocking, where variables that are highly dependent are updated jointly, can reduce auto-covariances significantly (see Figure 8). Each update of the Markov chain should of course also be implemented as efficiently as possible. Updates can sometimes be made more efficient by reformulating the model and introducing auxiliary variables that make conditional distributions easier to simulate from in a Gibbs sampler. Auxiliary variables were used in Paper I to make the posterior distribution of the latent field Gaussian.

To do inference for model (2), we want to construct a Markov chain  $((\mathbf{w}_i, \gamma_i))_{i=1}^n$  which has invariant distribution  $\mathbf{w}, \gamma \mid \mathbf{y}$ . This Markov chain can be used to approximate posterior marginal densities and posterior means. A simple algorithm for updating the Markov chain according to the invariant distribution is to use a Gibbs sampler with blocking that alternates between updating the hyper-parameters and the latent field. An update  $(\mathbf{w}_{n+1}, \gamma_{n+1}) \mid (\mathbf{w}_n, \gamma_n)$  can be done by first generating  $\gamma_{n+1}$  from the distribution of  $\gamma \mid \mathbf{w}_n, \mathbf{y}$ , and then generating  $\mathbf{w}_{n+1}$  from  $\mathbf{w} \mid \gamma_{n+1}, \mathbf{y}$ . The posterior density for the latent field  $\mathbf{w}$ , using that  $\pi(\mathbf{w} \mid \gamma, \mathbf{y}) \propto \pi(\mathbf{y}, \mathbf{w}, \gamma)$ , is

$$\pi(\mathbf{w} \mid \gamma, \mathbf{y}) = \alpha \exp \left( -\frac{(\mathbf{y} - \mathbf{w})^T (\mathbf{y} - \mathbf{w})}{2\sigma^2} - \frac{\mathbf{w}^T \mathbf{Q}(\gamma) \mathbf{w}}{2} \right),$$

where  $\alpha$  is a normalization constant. As the density for  $\mathbf{w} \mid \gamma, \mathbf{y}$  is a function of  $\mathbf{w}$  alone, only terms including  $\mathbf{w}$  have been kept. The posterior density in this case has the same form as a multivariate Gaussian density, and so the posterior distribution must be Gaussian with

$$\mathbf{w} \mid \gamma, \mathbf{y} \sim N(\hat{\mathbf{Q}}^{-1} \mathbf{y} / \sigma^2, \hat{\mathbf{Q}}^{-1}), \quad (5)$$

where  $\hat{\mathbf{Q}} = \mathbf{Q}(\gamma) + \mathbf{I} / \sigma^2$ . A similar posterior distribution was obtained for the latent field in Paper I. Updating latent fields for this type of hierarchical model can often be the most computationally expensive step of a Gibbs sampler. For likelihood-based inference methods in general, the usefulness of Gaussian random field approximations  $\mathbf{w}$  depends on how easy it is to evaluate densities of distributions such as (5). When  $\mathbf{w}$  is a GMRF approximation, we can use the sparsity of  $\hat{\mathbf{Q}}$ . In Paper I, not only the sparsity, but also a Kronecker-structure of  $\mathbf{Q}(\gamma)$

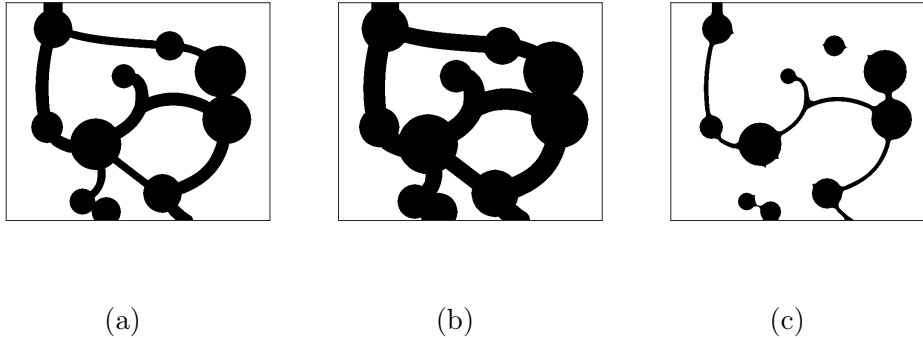


Figure 9: Illustration of erosion and dilation, using a circle structuring element  $B$ , with (a)  $\Phi$ , (b)  $\Phi \oplus B$  and (c)  $\Phi \ominus B$ .

that results from the separability of the Gaussian field model, was taken advantage of in order to make simulation from the posterior distribution of the latent field efficient.

### 3.2.2 Goodness of fit

Mathematical modelling often involves balancing model complexity with the efficiency of simulation and inference procedures that are available for the model. This is very much the case in spatial statistics, where computational costs of simulation, let alone inference, can be considerable.

There are many methods for assessing model fit. For a random set model  $\Phi$  with realizations that are subsets of  $T \subseteq \mathbb{R}^3$ , such as the model for the pore structure of EC/HPC polymer blends presented in Paper I, measuring goodness of fit involves characterizing the geometry of realizations of the fitted model, and comparing this characterization with data.

Basic characterization measures for stationary random sets defined on  $\mathbb{R}^3$ , are the volume fraction  $p$  and covariance  $k$ . Many characterization measures can also be obtained by transforming the random set using operations of mathematical morphology. The basic operations are dilation ( $\oplus$ ) and erosion ( $\ominus$ ), which are defined w.r.t. a structuring element  $B$  as

$$\Phi \oplus B = \{\mathbf{t} + \mathbf{s} : \mathbf{t} \in \Phi, \mathbf{s} \in B\},$$

and

$$\Phi \ominus B = \{\mathbf{t} \in \Phi : -B + \mathbf{t} \subseteq \Phi\}.$$

Dilation enlargens the set  $\Phi$  with the structuring element  $B$ , while erosion subtracts  $B$  from  $\Phi$ , see Figure 9. These operations were defined for random closed sets in Matheron (1975).

Dilation and erosion are used to characterize the shape of random sets. Popular measures obtainable using dilation and erosion are contact distribution functions, empty space functions and chord length distribution functions (Chiu et al., 2013, Ch. 6). Pore size distributions provide related measures of the shape of random sets. These are obtained as distributions of local pore sizes. Local pore sizes are defined w.r.t. structuring elements using the operation opening, which consists of an erosion followed by a dilation. The local pore size in a point

$\mathbf{t} \in \Phi$  is the size of the largest rescaled structuring element that fits within the set  $\Phi$  and which covers  $\mathbf{t}$ . More details about the definition of pore size distributions are given in Appendix B of Paper I. See also Figure 2, Paper III for an example of local pore sizes computed in a 2D pore structure. Measures related to local pore size were used in all five papers.

Whereas pore size distributions relates to local pore size, contact distribution functions can be seen as distributions of distances, computed using erosion w.r.t. the structuring element, to the boundary of the set  $\Phi$ . If the aim is to do a shape analysis of a random set, local pore sizes can be easier to interpret than distances to the boundary. It is on the other hand very difficult to obtain theoretical expressions for pore size distributions w.r.t. structuring elements other than lines (Matheron, 1975, pp. 175–176). Theoretical expressions for contact distribution functions have been obtained for many random set models, see Chiu et al. (2013, Ch. 6.3.3). For line structuring elements, the relationship between linear size distributions and linear contact distribution functions was derived in Matheron (1975, pp. 51–52). The linear contact distribution functions can in turn be related to chord length distribution functions, see Chiu et al. (2013, pp. 226–227).

The connectivity of the random set is also an important geometric characteristic. A connectivity measure called the two-point cluster function has been shown to encode more relevant information for reconstructing porous media than both high-order correlation functions and pore size related distribution functions (Torquato, 2010). The excursion sets used to assess the goodness-of-fit of numerically simulated diffusion in Paper I can also be seen as a connectivity measure. Connectivity measures that capture pore geometry properties important for understanding transport properties were used in Papers II-V, see the next section.

Other types of characterization measures are e.g. the Euler characteristic and related intrinsic volumes (Adler, 2000); functions determined by intrinsic volumes calculated for successive erosions/dilations of the set  $\Phi$  (Chiu et al., 2013, p. 229); and local distributions, which are distributions of geometric characteristics such as intrinsic volumes computed for subsets of the set  $\Phi$  (Hilfer, 2000).



## 4 Connecting pore geometry properties to diffusive transport

The diffusive transport rate through a porous material is determined by its pore geometry. Methods for characterizing properties of the pore geometry that have a significant impact on diffusive transport rates were developed in Papers II-V. The focus was on methods that capture the pore length and bottleneck effects. These factors and methods are discussed in detail in this section. Other properties, such as the prevalence of dead ends, could also have a significant impact on diffusive transport rates, but were not considered in this thesis.

The focus in this thesis has been on predictors that have a clear interpretation in terms of the pore geometry. Other methods that have been used in the context of connecting pore geometry to diffusive transport rates, or the mathematically equivalent properties of electrical conductivity and heat conductivity (Torquato, 2002), are the high-order correlation functions used in e.g. Liasneuski et al. (2014).

### 4.1 Diffusion

Diffusive transport is driven by random movement of particles, where each particle moves according to Brownian motion. The diffusive flux  $\mathbf{J} = (J_x, J_y, J_z)$ , where  $J_x$  gives the net amount of particles transported in the  $x$ -direction per unit area and time,  $J_y$  the net amount transported in the  $y$ -direction, and  $J_z$  the net amount transported in the  $z$ -direction, is proportional to the negative concentration gradient as

$$\mathbf{J} = -D_0 \nabla c. \quad (6)$$

Here  $\nabla = (\frac{\partial}{\partial x}, \frac{\partial}{\partial y}, \frac{\partial}{\partial z})$ ,  $c$  is the particle concentration and  $D_0$  is the diffusion coefficient. Random particle movement thus results in a net transport of particles from domains with higher concentration to domains with lower concentration. The mass conservation law, which implies that the rate of change  $\frac{\partial c}{\partial t}$  should equal  $\nabla \cdot \mathbf{J}$ , gives that

$$\frac{\partial c}{\partial t} = -D_0 \Delta c, \quad (7)$$

for constant  $D_0$ , which is the well-known heat equation. Here  $\Delta = \frac{\partial^2}{\partial x^2} + \frac{\partial^2}{\partial y^2} + \frac{\partial^2}{\partial z^2}$  is the Laplace operator.

We model the diffusive transport in pore structures as having fixed concentrations  $c_{\text{inlet}}$  at the inlet ( $z = 0$ ) and  $c_{\text{outlet}}$  at the outlet ( $z = L_z$ ) of the pore structure. This corresponds to

high concentration of drug in the core of the pellet and low concentration on the outside of the pellet, in the case of controlled drug release. The concentration difference drives diffusive transport from inlet to outlet. Since there is no transport in or out of pore walls, the boundary conditions  $\mathbf{J} \cdot \mathbf{n} = -D_0 \nabla c \cdot \mathbf{n} = 0$  are imposed at the walls, where  $\mathbf{n}$  is a vector normal to the wall. The steady state solution  $c$  satisfies  $\frac{\partial c}{\partial t} = 0$ , is zero in the matrix (solid part of the pore structure) and satisfies (7) in the pore space, with the described boundary equations.

In Paper II and Paper V the software Gesualdo (Gebäck and Heintz, 2014) was used to solve (7) numerically. Gesualdo uses the lattice Boltzmann method, which simulates particle movement and interaction at a level of abstraction above the particle level using particle distributions on regular lattices. These computations can easily be parallelized, which makes the lattice Boltzmann method attractive for large-scale simulations. An alternative is to simulate diffusion on the particle level, called molecular dynamics simulations. This can however be very computationally demanding, as large number of particles need to be simulated (Mohamad, 2011). The finite element method, described in Chapter 3.1.2, is a popular method for solving PDEs approximately. An advantage when using the lattice Boltzmann method is that mass conservation can be enforced, which is difficult when using the finite element method (Hughes et al., 2000). Finite volume methods are other alternatives, which similarly to the finite element method approximates solutions to the PDE (7) directly, instead of simulating particle dynamics, but which can also enforce mass conservation (Eymard et al., 2000). Network models, which can be seen as a kind of finite volume method where the dynamics are modelled on the pore level, is another option. This method is less exact than other methods, but is efficient and can be used for large pore systems (Blunt et al., 2013).

When explaining diffusive transport in terms of the pore geometry, we are interested in the steady state transport  $\mathbf{J}$  through the pore structure. We define the effective diffusion coefficient  $D_{\text{eff}}$  by

$$\langle J_z \rangle = -D_{\text{eff}} \tilde{\nabla} c$$

following Gebäck et al. (2015). Here  $\langle \cdot \rangle$  denotes the average taken over the whole pore structure,  $\tilde{\nabla} c = (c_{\text{inlet}} - c_{\text{outlet}})/L_z$ , and  $L_z$  denotes the length of the pore structure in the  $z$ -direction. The effective diffusion coefficient maps the applied concentration gradient over the whole pore structure  $\tilde{\nabla} c$  to the mean diffusive transport  $\langle J_z \rangle$  through the structure, in the same way as the diffusion coefficient maps the local concentration gradient to the flux in equation (6).

Let  $\mathbf{J}$  be the flux of the steady state solution in a given pore structure, with concentration-boundary condition  $(c_{\text{inlet}}, c_{\text{outlet}})$ . By the linearity of equations (6) and (7) and the boundary conditions, keeping the pore structure constant but changing the concentration-boundary condition to  $(c'_{\text{inlet}}, c'_{\text{outlet}})$ , where  $c'_{\text{inlet}} - c'_{\text{outlet}} = \alpha(c_{\text{inlet}} - c_{\text{outlet}})$ , leads to a rescaled solution  $\alpha\mathbf{J}$ . Similarly, rescaling the pore geometry by  $\alpha$ , but keeping the concentration-boundary condition constant, leads to a rescaled solution  $\mathbf{J}/\alpha$ . Furthermore, the average of the steady state flux in the  $z$ -direction taken over the whole structure equals the average over any slice in the  $x, y$ -plane, due to mass-conservation. Thus  $T = A\langle J_z \rangle$ , where  $T$  is the total transport per unit time through the pore structure and  $A$  is the area of a slice in the  $x, y$ -plane. The effective diffusion coefficient is therefore proportional to the total transport per unit time, but is independent of the concentration-boundary condition and of the size of the pore structure.

The rescaled coefficient  $D_{\text{eff}}/D_0$  is often used, see e.g. Ghanbarian et al. (2013); Stenzel et al. (2016).  $D_{\text{eff}}/D_0$  can be seen as the reduction in transport rate compared to a structure with no pore matrix, i.e. with only free diffusion. The transport ratio, defined as

$$TR = \frac{D_{\text{eff}}}{\epsilon D_0},$$

was used in Paper II and Paper V. Here  $\epsilon$  denotes the pore volume fraction. It holds that  $TR \leq 1$  by the Wiener bounds (Wiener, 1912), and  $TR$  can be rewritten as the ratio between the total transport through the pore structure and the total transport through an optimal pore structure with the same pore volume fraction, see Paper II. An optimal pore structure is a pore structure which has the highest possible transport rate for a given pore volume fraction, which is a pore structure with straight pores aligned with the  $z$ -direction. Similarly, the relative flux  $\mathbf{J}/(D_0 \tilde{\nabla} c)$  was used in Paper II and Paper V (termed normalized flux in Paper II) for ease of interpretation. Here  $D_0 \tilde{\nabla} c$  is the norm of the flux through an optimal pore structure of any pore volume fraction. The flux through an optimal pore structure  $\mathbf{J}_{\text{opt}}$  equals the flux  $\mathbf{J}_{\text{free}}$  of free diffusion in a volume with the same applied concentration gradient  $\tilde{\nabla} c$ , which is  $\mathbf{J}_{\text{free}} = (0, 0, -D_0 \tilde{\nabla} c)$ .

#### 4.1.1 Bounds

It holds that  $TR \leq 1$  generally, as noted above and in Paper II. Other upper and lower bounds have also been derived using similar methods. Here are some examples, given with respect to the transport ratio:

Maxwell's formula (Maxwell, 1881, Chap. 9, p. 403),  $TR = \frac{1}{1 + \frac{1}{2}(1-\epsilon)}$ , was derived for a dilute suspension of spheres as  $\epsilon \rightarrow 1$ . It was shown in Hashin and Shtrikman (1962) that this is an upper bound which is valid for all isotropic geometries for any value of  $\epsilon$ , and it is the strictest upper bound obtainable using only the pore volume. The corresponding lower bound using only the pore volume is zero. Stricter bounds, both upper and lower, can be found by adding more information about the pore geometry, see Torquato (1991). The isotropic assumption can also be relaxed. As an example of a stricter upper bound,  $TR \leq \frac{1}{1 - \frac{1}{2} \ln \epsilon}$  holds for overlapping spheres with Poisson distributed centers and uniform or random radii (Weissberg, 1963).

## 4.2 Important pore geometry factors

Two pore geometry-properties that are thought to be important for determining the rate of diffusive transport through a pore structure are the length of paths through the pores and possible bottleneck effects (Siepmann et al., 2012, Ch. 9). Long paths and/or the presence of bottlenecks lead to low transport rates. These effects are illustrated in Figure 10. It can be helpful to think of diffusion dynamics in terms of the concentration  $c$ , as diffusive flux  $\mathbf{J}$  is driven by a concentration gradient by (6). The most effective pore structure in terms of mean transport, for a given pore volume, has straight pores aligned with the direction of transport, such as the pore structure shown in the left of the figure. If we consider transport through a winding, or tortuous, pore (middle pore structure), the concentration gradient is reduced due

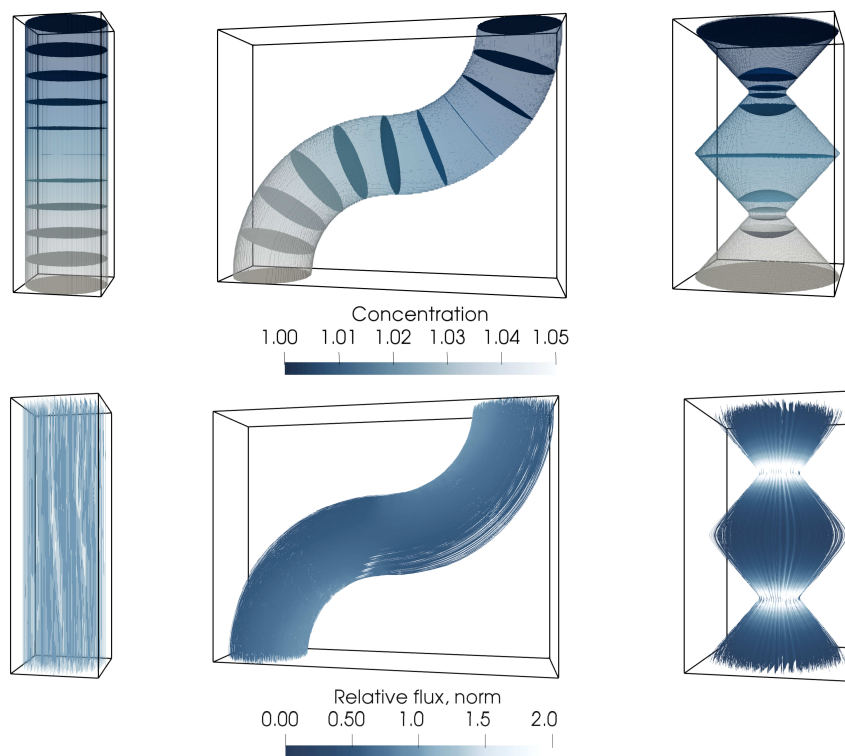


Figure 10: Steady state solutions computed by Gesualdo, showing concentration  $c$  (top row) and corresponding streamlines colored by norm of relative diffusive flux (bottom row), for three simple pores. 11 isolines of  $c$  at regularly spaced distances in the interval  $[c_{\text{outlet}}, c_{\text{inlet}}] = [1.0, 1.5]$  are shown, colored by the value of the concentration. Transport was computed from top to bottom, i.e. the inlet is at the top and the outlet is at the bottom. The color-scale of normalized flux was cut off at 2.0.

to the increased length of the pore, decreasing the transport. The concentration gradient field of the pore with varying pore size (right pore structure), can be seen to be less efficient than that of a straight pore due to the large concentration drop at the two pore necks. In these examples, the tortuous pore and the pore with varying pore size have about the same transport efficiency in terms of the transport ratio, with  $TR = 0.43$  and  $TR = 0.48$ , respectively. Both increased pore length and variation in pore size was taken into account in Papers II-V.

More complex pore structures present another type of bottleneck effect, caused by many paths converging in the same pore. An 2-d pore structure with bottlenecks of this kind is shown in Figure 11. The transport efficiency is considerably lower in the complex pore structure compared to the pores shown in Figure 10, with  $TR = 0.17$ . This is because, as can be seen from the streamlines of relative flux, there is a large portion of the pore structure through which there is very little transport. The example pore structure in Figure 11 was taken from Paper V, where this bottleneck effect was studied. This type of bottleneck was also found in one of the pore structures obtained from FIB-SEM images of the coating material presented in Paper III and Paper IV.

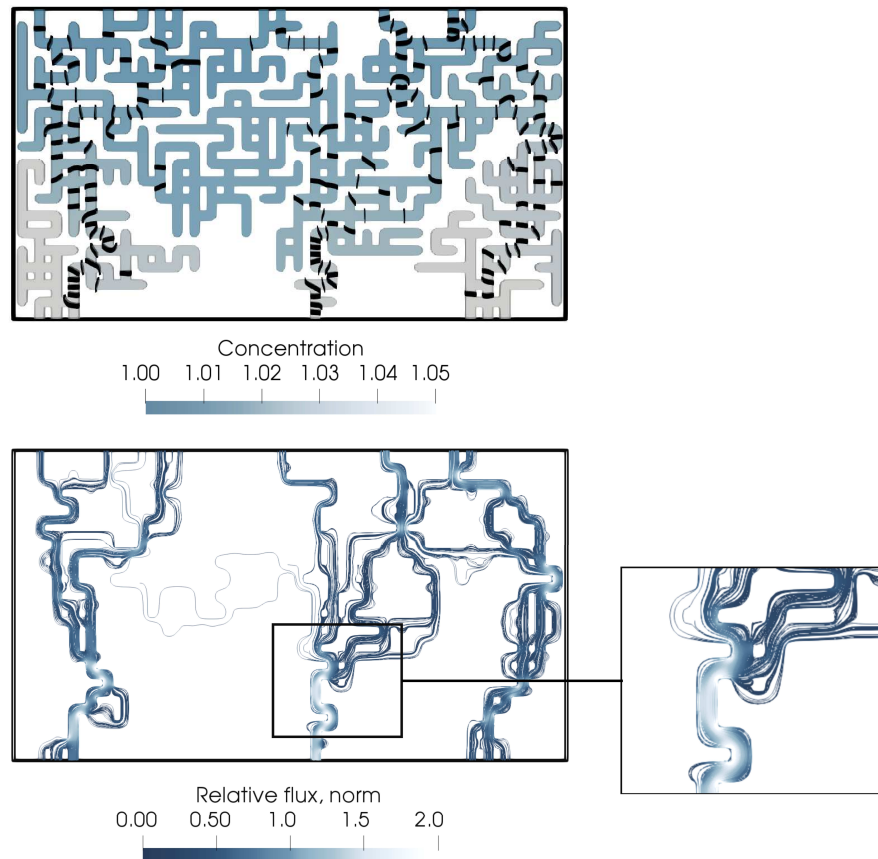


Figure 11: A steady state solution computed by Gesualdo, showing concentration  $c$  (top row) and corresponding streamlines colored by norm of relative diffusive flux (bottom row), for a simple 2-d pore structure. 31 isosurfaces of  $c$  at regularly spaced distances in the interval  $[c_{\text{outlet}}, c_{\text{inlet}}] = [1.0, 1.5]$  are shown in black. An area with a strong bottleneck effect is zoomed in on. Transport was computed from bottom to top, i.e. the inlet is at the top and the outlet is at the bottom. The color-scale of normalized flux was cut off at 2.0.

#### 4.2.1 Simple sectioned model for diffusion in a single pore

Simple models for steady state solutions can be useful for the understanding of the relationship between pore geometry and transport. The simple sectioned model developed in this section is based on similar arguments as presented in e.g. Currie (1960). A similar simple model was used in Paper II and Paper V for the special case of a tortuous tube with constant cross-section. Whereas the simple model from Paper II and Paper V can be used to draw conclusions about how path length influences diffusive transport, the simple sectioned model can be used to draw conclusions about the influence of bottleneck effects, and the influence of the interplay between path length and bottleneck effects, as discussed in the end of this section.

The simple sectioned model is obtained by dividing a pore into  $n$  sections  $Sec_1, \dots, Sec_n$ , as illustrated in Figure 12. To each section  $Sec_i$  is associated a length  $L_i$ , measured in the

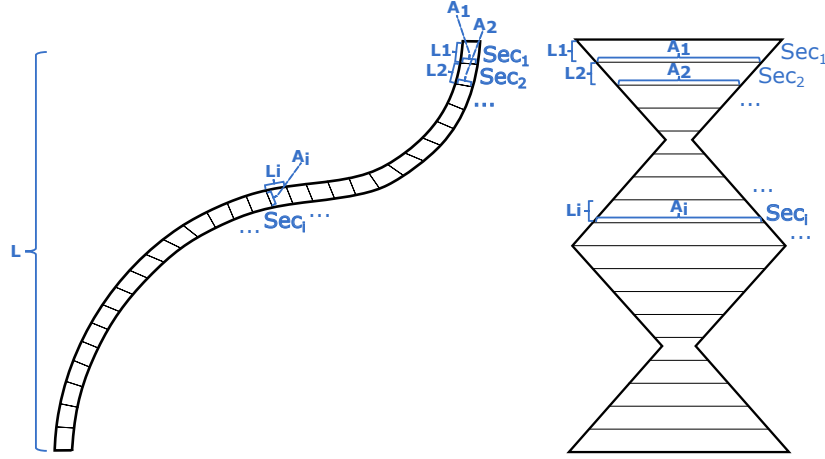


Figure 12: Illustration of the setup of the simple model, showing two pores with the division into sections  $Sec_i$ , the cross-sectional area  $A_i$  and the length  $L_i$  of each section, and the height  $L$  of the two pores.

transport direction through the section, and the cross-sectional area  $A_i$  of a plane (or length of a line for a pore in 2D), which is defined to be perpendicular to the transport direction (black lines dividing the two pores into sections in Figure 12). The total transport through  $Sec_i$  is then assumed to equal the total transport through a straight pore with length  $L_i$  and base-area  $A_i$ . By the principle of mass conservation, the total transport per unit time,  $T$ , should be the same for all sections. Let  $c_{i-1}$  and  $c_i$  be the concentration at the inlet and outlet, respectively, of section  $Sec_i$ . To satisfy the concentration boundary conditions,  $c_0 = c_{\text{inlet}}$  and  $c_n = c_{\text{outlet}}$ .

*Transport through section  $Sec_i$ :* The total transport through section  $Sec_i$  is a function of the unknown concentration difference, as the flux in a straight pore of length  $L_i$  with concentration difference  $c_i - c_{i-1}$  is  $\mathbf{J}_{\text{free}} = (0, 0, -D_0(c_i - c_{i-1})/L_i)$ . Thus the total transport through section  $Sec_i$  is  $T = -A_i D_0(c_i - c_{i-1})/L_i$ . We define  $R_i = L_i/(D_0 A_i)$  in analogy with Ohm's law<sup>3</sup>, and so

$$T = -\frac{c_i - c_{i-1}}{R_i}. \quad (8)$$

*Mass conservation:* As equation (8) holds for all  $i$  by the principle of mass conservation, we have that

$$\frac{c_i - c_{i-1}}{R_i} = \frac{c_j - c_{j-1}}{R_j}, \quad \forall i, j. \quad (9)$$

Using that  $\sum_i c_i - c_{i-1} = c_n - c_0 = c_{\text{inlet}} - c_{\text{outlet}}$ , the solution  $(c_0, c_1, \dots, c_n)$  is given by the

<sup>3</sup>Ohm's law states that  $I = V/R$ , where  $I$  is the current,  $V$  is the voltage and  $R$  is the resistance. As the equations governing electrical conductance and diffusive transport are the same, we write  $T = -(c_{\text{inlet}} - c_{\text{outlet}})/R$ , where the total transport per unit time  $T$  corresponds to the current and the concentration difference  $c_{\text{inlet}} - c_{\text{outlet}}$  corresponds to the voltage.

set of equations

$$c_i - c_{i-1} = \frac{R_i}{\sum_j R_j} (c_{\text{inlet}} - c_{\text{outlet}}), \quad i \in \{1, \dots, n\}.$$

The total transport given this *simple sectioned model* is then

$$T = -\frac{1}{\sum_j R_j} (c_{\text{inlet}} - c_{\text{outlet}}). \quad (10)$$

Thus we have that  $T = -(c_{\text{inlet}} - c_{\text{outlet}})/R$  in analogy with Ohm's law, where  $R = R_1 + \dots + R_n$ . This fits with the formula  $R = R_1 + \dots + R_n$  for the resistance of an electric circuit with  $n$  resistors connected in series (Cutnell and Johnson, 2018, p. 552), with  $R_i$  being the resistance of the  $i$ :th resistor. A similar formula has been used to compute the diffusion coefficient of a composite material composed of  $n$  sheets, namely  $l/D_{\text{eff}} = l_1/D_1 + \dots + l_n/D_n$ , with  $l_i$  being the thickness and  $D_i$  being the diffusion coefficient of the  $i$ :th sheet and  $l$  being the thickness and  $D_{\text{eff}}$  being the effective diffusion coefficient of the composite, and has also been used when  $D_i$  is the effective diffusion coefficient of the  $i$ :th sheet (Bell and Crank, 1974). A similar model was applied to a tube of constant cross-sectional area and to a pore of sinusoidal shape in Currie (1960), although there the resistance  $R$  was defined using an integral over  $1/A(z)$ , where  $A(z)$  was the area of the cross-section at position  $z$ .

The total transport (10) obtained from the simple sectioned model seems to fit reasonably well for simple pore such as those pictured in Figure 12. For a pore with constant cross-section area, such as the tortuous pore shown on the left in the figure, i.e. for a pore with  $A_i = A_j =: A$ , the total transport obtained using the simple sectioned model reduces to

$$T = \frac{A}{\tau_{\text{simple}}} J_{\text{free},z}.$$

Here  $\tau_{\text{simple}} = \sum_j L_j/L$ ,  $L$  is the height of the pore as indicated in the figure, and  $\mathbf{J}_{\text{free}}$  is the flux of free diffusion with the same applied concentration gradient  $(c_{\text{inlet}} - c_{\text{outlet}})/L$ .  $\tau_{\text{simple}}$  is thus a measure of how much longer the pore is compared to the height of the pore. The total transport through a straight pore with cross-sectional area  $A$  is  $AJ_{\text{free},z}$ . Thus, compared to a straight pore with the same cross-sectional area  $A$  as the tortuous pore, the total transport is reduced by a factor  $1/\tau_{\text{simple}}$ . Compared to a straight pore with the same pore volume as the tortuous pore, which has cross-sectional area  $\tau A$ , the total transport is reduced by a factor  $1/\tau_{\text{simple}}^2$ , thus

$$TR = \frac{1}{\tau_{\text{simple}}^2}. \quad (11)$$

Note that the simple sectioned model gives correct transport ratio  $TR = 1$  for straight pores with constant cross-sectional area. The same transport ratio as that given in (11) was obtained in Currie (1960) and in Paper II, using similar arguments which were based on approximating the transport through a tilted pore with constant cross-sectional area with the transport through

a straight pore with the same length and cross-sectional area<sup>4</sup>. The exponent of  $1/\tau$  in (11) has sometimes been claimed to be 1, not 2, in e.g. Petersen (1958) and Holzer et al. (2013b), see Paper II. The model (11) for the transport ratio was tested in Paper V however, and was found to fit well with numerically simulated diffusion in tortuous pores.

For a pore with constant section length  $L_i = L_j =: L_{\text{sec}}$ , the total transport (10) obtained using the simple sectioned model reduces to

$$T = \frac{1}{\tau_{\text{simple}} \langle \frac{1}{A_j} \rangle} J_{\text{free},z},$$

where  $\langle \cdot \rangle$  denotes the average,  $\tau_{\text{simple}} = \sum_j L_j/L$  with  $L$  being the height of the pore as indicated in the Figure 12, and  $\mathbf{J}_{\text{free}}$  denotes the flux of free diffusion with the same applied concentration gradient  $(c_{\text{inlet}} - c_{\text{outlet}})/L$ .  $\tau_{\text{simple}}$  is thus a measure of how much longer the pore is compared to the height of the pore. The total transport through a straight pore with the same pore volume as the pore with constant section length is  $\tau_{\text{simple}} \langle A_j \rangle J_{\text{free},z}$ , since the cross-sectional area of the straight pore is  $\tau_{\text{simple}} \langle A_j \rangle$ , and so

$$TR = \frac{1}{\tau_{\text{simple}}^2 \langle \frac{1}{A_j} \rangle \langle A_j \rangle}. \quad (12)$$

A similar model was obtained in Currie (1960) for the special case of a sinusoidal pore and in Berg (2012).

The transport ratio given by (12) is invariant to rescaling the pore, as is the true transport ratio. It is not obvious from (12) that  $TR \leq 1$ , though the inequality clearly holds when  $\langle \frac{1}{A_j} \rangle \langle A_j \rangle = 1$ . It is easy to show however for  $n = 2$  by using a change of variable to  $x = A_1/A_2$ , in which case the transport ratio for a given relative pore length  $\tau_{\text{simple}}$  is maximized for  $A_1/A_2 = 1$ , i.e. for a pore with constant cross-sectional area. By applying the simple sectioned model iteratively to two sections at a time, the inequality  $TR \leq 1$  can be shown to hold for any  $n$ . Thus the inequality holds for  $TR$  obtained using the simple sectioned model, just as it holds for the true solution to the diffusion equations by the Wiener bounds (Wiener, 1912).

The explicit dependence of the transport ratio on the two factors  $\tau_{\text{simple}}$  and  $\langle \frac{1}{A_j} \rangle \langle A_j \rangle$ , respectively, is shown in Figure 13. The total transport is e.g. equally reduced, with  $TR = 0.5$ , for a pore with constant cross-sections for which  $\tau_{\text{simple}} = \sqrt{2}$  as for a straight pore for which  $A_1/A_2 = 0.17$ , though the transport reduction is a result of two different mechanisms: Suppose that  $L_i = L_j =: L_{\text{sec}}$ . Firstly, the concentration difference is the same for all sections for a pore with constant cross-sections, and so the reduction in total transport comes from the reduction in concentration difference compared to sections of a straight pore. The results for the tortuous pore shown in the middle of Figure 10 shows that this is a reasonable approximation to the steady state solution computed using Gesualdo. Secondly, as can be seen from the set of equations (9), the concentration difference  $c_i - c_{i-1}$  is greater for a section with a relatively

---

<sup>4</sup>Note that here a straight pore refers to a pore with constant cross-sectional area that is aligned with the direction of transport, such as the pore to the left in Figure 10, as was done in Currie (1960) where the same model was obtained. In Paper II a straight pore referred to a possibly tilted pore with constant cross-sectional area.

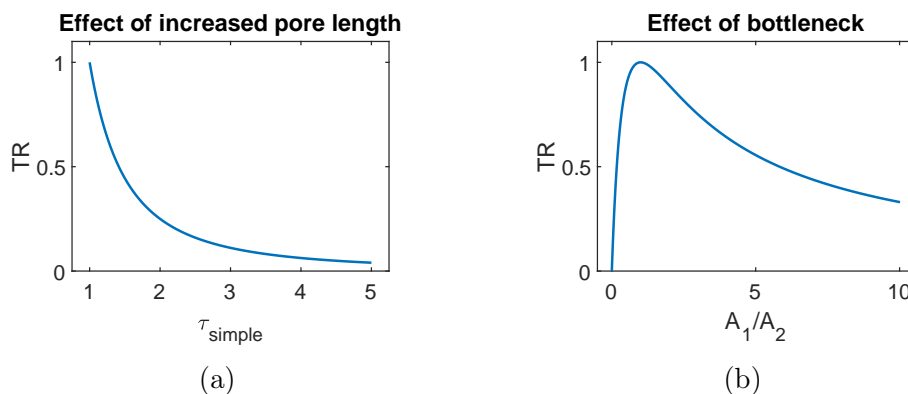


Figure 13: Illustration of the transport ratio computed using the simple sectioned model. (a) The transport ratio computed using the model (11), i.e. the transport ratio of a pore with constant pore size but increased pore length. (b) The transport ratio computed using the model (12) with  $n = 2$  and  $\tau_{\text{simple}} = 1$ , i.e. the transport ratio of a straight pore with varying pore size, where  $A_1/A_2$  is the ratio between the cross-sectional area of the first section and the cross-sectional area of the second section of the pore. The maximum transport ratio  $TR = 1$  is attained at  $A_1/A_2 = 1$ .

small cross-sectional area  $A_i$ . This means that a relatively large portion of the total drop in concentration  $c_{\text{outlet}} - c_{\text{inlet}}$  has to be “spent” at section  $Sec_i$ . This is intuitive, since the flux through a section with small cross-sectional area has to be higher than the flux through a section with larger cross-sectional area in order for the transport through the two sections to be the same, and the flux is proportional to the concentration gradient. A large drop in concentration can also be observed at the two bottlenecks in the pore with varying pore size shown in Figure 10, as the iso-surfaces are clustered around the bottlenecks. The iso-surfaces are not flat surfaces oriented orthogonally to the transport direction though, as is assumed in the simple sectioned model.

The simple sectioned model for  $TR$  in (12) is only formulated for a single pore, and therefore does not address bottleneck effects caused by many paths converging in the same pore, such as in the pore structure shown in Figure 11 and in the data considered in Papers III-V. The same principle should apply in this case though, i.e. a relatively large portion of the total drop in concentration has to be “spent” at the bottleneck leading to a reduction in total transport. Big concentration drops can be observed at the bottlenecks in the pore with varying pore size in Figure 11.

### 4.3 Pore geometry measures

The factors identified as important determinants of diffusive transport in the last section were (1) the length of a pore, or in the case of more complex pore structures the length of paths through the porous network, (2) bottlenecks caused by variation in pore size and (3) bottlenecks caused by many paths converging in the same pore. Available methods to characterize the first two factors are presented in the following two sections. Methods to characterize the third factor

were developed in Paper III and V.

### 4.3.1 Path lengths

Path lengths through the pore structure can be computed as the length of geodesic paths. Here, a geodesic path  $GeoPath_{dir}(p)$  corresponding to the point  $p$  in the pore space is the shortest path that lies completely in the pore space and that connects the inlet and outlet to the point  $p$ . The inlet and outlet are defined as the faces at the edge of the pore structure in the direction  $dir$ , with  $dir = x, y$  or  $z$ . Examples of geodesic paths in a 2-d pore structure can be found in Figure 1, Paper III and Figure 2, Paper IV. Geodesic paths were used in Paper IV to visually explore the connectivity of pore structures obtained from microscopy images of the coating material.

The length of the geodesic path is often given relative to the height of the pore structure, i.e. as the geodesic tortuosity  $\tau(p) = l(GeoPath_{dir}(p))/L$ , where  $l(GeoPath_{dir}(p))$  is the length of the geodesic path and  $L$  is the height of the pore structure in direction  $dir$ . 2-d examples illustrating the tortuosity can be found in Figure 2, Paper III. The geodesic tortuosity is described in e.g. Adler (1992); Brémond et al. (1994); Lindquist et al. (1996); Thiedmann et al. (2009); Peyrega and Jeulin (2013); Pecho et al. (2015); Stenzel et al. (2016, 2017); Neumann et al. (2019); and Chaniot et al. (2019). The geodesic tortuosity is sometimes called geometric tortuosity and can also be computed from a skeleton representation of the pore structure. The geodesic tortuosity was shown in Brémond et al. (1994); Stenzel et al. (2016, 2017) to be a good predictor of diffusive transport rates and the equivalent property of electrical conduction. In Paper II, a tortuosity factor was defined in such a way that the model (11) holds for pore structures consisting of separate tubes of constant cross-sectional areas. The tortuosity factor and standard deviation of the point-wise tortuosity  $\tau(p)$ , for points  $p$  in the pore space, was used in Paper II and Paper V to predict diffusion. In Paper III and Paper IV the point-wise tortuosities  $\tau(p)$  were used to characterize the connectivity of the coating material.

The tortuosity has sometimes been defined using the model (11), and is then thought to capture the increased length of streamlines of diffusive flux compared to the height of the pore structure. This definition of the tortuosity, sometimes called the diffusive tortuosity, is commonly used (Ghanbarian et al., 2013, p. 1464). This however assumes that the only factor that reduce the transport rate are increased path lengths, as discussed in Paper II. Another type of tortuosity, the hydraulic tortuosity, is computed as the length of streamlines of flow (Duda et al., 2011).

### 4.3.2 Bottleneck effects

Bottlenecks caused by variations of pore size, such as can be observed in the pore structure in the right of Figure 10, were identified as important factors reducing diffusive transport rates in Owen (1952) and Petersen (1958). Methods for characterizing this type of bottleneck in complex pore structures can be found in Holzer et al. (2013b) and Berg (2012). In Berg (2012), a constriction factor similar to the factor  $1/(\langle \frac{1}{A_j} \rangle \langle A_j \rangle)$  from model (12) was used. In Holzer et al. (2013b), the median mercury intrusion porosimetry (MIP)-pore size was used to characterize the size of bottlenecks. The MIP-pore size is computed similarly to the local pore

size using successive erosions and dilations (see Figure 9), with the difference that connectivity is also taken into account. See Figure 2, Paper III, for a 2-d example of the MIP-pore size. The constrictivity was defined in Holzer et al. (2013b) as the ratio between the median MIP-pore size and the median local pore size, and have been used e.g. in Stenzel et al. (2016, 2017); Holzer et al. (2013a) and Neumann et al. (2016). See Paper II and Paper III for more details about the constrictivity, which was used in Paper II, Paper III and Paper V.

A new measure that captures bottleneck effects caused by many paths converging in the same pore, such as can be observed in Figure 11, was introduced in Paper III. This measure, termed the geodesic channel-strength, was computed from geodesic paths and was used in Papers III-V (see Figure 1, Paper III, Figure 3, Paper IV and Figure 1, Paper V, for 2-d examples of the geodesic channel-strength). This kind of bottleneck, illustrated in Figure 11 above, is not captured by the existing methods based on constrictivity described above.

#### 4.4 Multiplicative regression models for predicting diffusion

The model (12) for  $TR$  obtained from the simple sectioned model indicate that a multiplicative regression model of the form

$$TR = Pred_1^{\beta_1} \dots Pred_n^{\beta_n} \quad (13)$$

could be a good prediction model for the transport ratio, with model parameters  $\beta_1, \dots, \beta_n$ , and with predictors  $Pred_1, \dots, Pred_n$  that take values in the unit interval  $[0, 1]$  since  $TR \in [0, 1]$ . The model (12) then corresponds to  $Pred_1 = 1/\tau_{\text{simple}}$  and  $Pred_2 = 1/(\langle \frac{1}{A_j} \rangle \langle A_j \rangle)$ , with  $\beta_1 = 2$  and  $\beta_2 = 1$ .

A short review of multiplicative regression models that have been used to predict diffusive transport measures such as  $D_{\text{eff}}$  and  $TR$  can be found in Paper II. The pore volume fraction  $\epsilon$ , the geodesic tortuosity  $\tau$  and the constrictivity were used as predictors in these regression models. Multiplicative regression models were fitted to diffusive transport results computed numerically using Gesualdo in Paper II and Paper V, following Stenzel et al. (2016), but with the addition of more predictors. Both papers examine the effect of fixing the exponent to the theoretical value 2 in order for the model to fit with the simple pore structures for which model (11) applies, but there is more emphasis on this aspect of the modelling in Paper V.



## 5 Summary of appended papers

### 5.1 Paper I

In Paper I a stationary Gaussian random field based model for the pore structure of the EC/HPC coating material was fitted to parts of two sets of CLSM images from Häbel et al. (2017), i.e. two 3-D images, corresponding to two EC/HPC films. The sets of CLSM images were binarized using a threshold that was a function of the depth to account for a signal decrease with depth. Parts of the CLSM images for which the stationarity assumption was reasonable were chosen, which resulted in 3-D samples that were smaller in the  $z$ -direction compared to in the  $\mathbf{t} = (x, y)$ -planar sections. Each sample was represented as a vector,  $\mathbf{y} = (y_1, \dots, y_m)$ , where  $m$  equalled the number of voxels in the sample. The model for  $\mathbf{y} = (y_1, \dots, y_m)$  was formulated as

$$y_i = \begin{cases} 1, & \text{if } X(\mathbf{t}_i, z_i) + \varepsilon_i \geq u, \\ 0, & \text{otherwise,} \end{cases} \quad i = 1, \dots, m, \quad (14)$$

for a threshold  $u \in \mathbb{R}$  (model (1) of Paper I, with  $\mathbf{s}$  replaced by  $\mathbf{t}$ ). Here  $\varepsilon_i$  are independent standard Gaussian random variables and  $X$  is a Gaussian field belonging to a family of Gaussian fields defined by a coupled system of SPDEs. This family has separable covariance functions  $C$ , i.e. covariance functions which can be written as  $C = C_z C_{\mathbf{t}}$ , with  $C_{\mathbf{t}}$  and  $C_z$  covariances of the oscillating Matérn fields mentioned in Chapter 3.1.3 (see also Figures 3 and 4, Paper I).  $\mathbf{t} = (x, y)$  correspond to planar sections of the EC/HPC coating material orthogonal to the direction of diffusive transport, which is represented by the  $z$ -axis. The separable covariance models the anisotropy of the CLSM images, where a different structure in the  $\mathbf{t}$ -planar sections compared to along the  $z$ -axis can be seen.

For computational efficiency, the Gaussian field in model (14) was replaced by the corresponding FEM approximation (see Section 3.1.2), defined by the GMRF  $\mathbf{w}$ , and the model was replaced by:

$$\begin{aligned} y_i \mid \mathbf{w}, u &\sim Be(\Phi(\mathbf{A}_{i,\bullet} \mathbf{w} - u)), \quad i = 1, \dots, m, \\ \mathbf{w} \mid \boldsymbol{\gamma} &\sim \mathbf{N}(0, \mathbf{Q}(\boldsymbol{\gamma})^{-1}), \\ \boldsymbol{\gamma} &\sim \pi(\boldsymbol{\gamma}), \\ u &\sim \pi(u). \end{aligned} \quad (15)$$

which is model (4) of Paper I (with misprint corrected). Here  $Be$  denotes the Bernoulli distribution,  $\Phi$  denotes the distribution function of a standard normal random variable, and  $\pi(\boldsymbol{\gamma})$  and

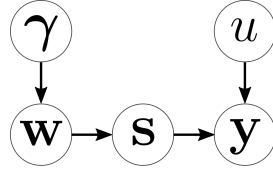


Figure 14: Graphical representation of the augmented model.

$\pi(u)$  are prior distributions for the parameters and the threshold, respectively. The precision matrix  $\mathbf{Q}$  can be written as a Kronecker product  $\mathbf{Q}_z \otimes \mathbf{Q}_t$ , due to the separability of  $C$ .

The binarized CLSM samples  $\mathbf{y}_{\text{CLSM}}$ , and the corresponding samples  $\mathbf{y}$  obtained from the model (15), were filtered to remove the noise, resulting in a model

$$\tilde{\mathbf{y}} = F(\mathbf{y}) \quad (16)$$

for the pore structure of the leached EC/HPC material. This is model (2) of Paper I.

A blocked Metropolis-within-Gibbs sampler was presented for fitting model (15) to CLSM images. Updating the latent GMRF by sampling from its conditional distribution was the most computationally expensive step in updating the Markov chain. Several methods were used to increase the efficiency of this step: (1) Auxiliary variables  $\mathbf{s}$ , the sum of the FEM approximation evaluated at the voxels of the CLSM image plus independent noise, were introduced. The conditional dependence structure of the augmented model is illustrated in Figure 14. These auxiliary variables made the conditional distribution of  $\mathbf{w} \mid \mathbf{s}, \gamma, u, \mathbf{y} \sim \mathcal{N}(\hat{\mathbf{Q}}^{-1} \mathbf{A}^\top \mathbf{s} / \sigma^2, \hat{\mathbf{Q}}^{-1})$ , i.e. multivariate Gaussian. (2) Samples from this (approximate) distribution were generated without computing full Cholesky factors of the precision matrix  $\hat{\mathbf{Q}}$  by taking advantage of the Kronecker structure of  $\mathbf{Q}(\gamma)$ , using the method introduced in Papandreou and Yuille (2010). (3) The method from Papandreou and Yuille (2010) was adapted so that the full matrix  $\mathbf{Q}(\gamma)$  did not need to be stored. This was done by taking advantage of the Kronecker structure of the precision matrix, solving the system  $(\mathbf{Q}_z \otimes \mathbf{Q}_t)^{-1} \mathbf{b}$  using operations on the matrices  $\mathbf{Q}_z$  and  $\mathbf{Q}_t$  alone, see Buis and Dyksen (1996), and has to the best of our knowledge not been used in the context of fitting GMRF based models before. This reduced the amount of elements stored in the MCMC algorithm from  $\mathcal{O}(n_z^2 n_t^2)$  to  $\mathcal{O}(n_z^2 + n_t^2)$ , where  $n_z$  and  $n_t$  denote the number of voxels in the  $z$ -direction and  $t$ -plane of the CLSM image, respectively. This significantly increased the size of the dataset the model could be fitted to. The feasible size of simulations from the model using the Cholesky factors also increased: on a laptop with 16GB RAM, samples larger than  $600 \times 600 \times 600$  could be generated (compare with the sizes given in Chapter 3.1.2). A more detailed description of the algorithm can be found in the section ‘‘The MCMC algorithm’’ in the appendix of Paper I, and a more detailed description of the methods for taking advantage of the Kronecker structure of  $\mathbf{Q}(\gamma)$  can be found in the section ‘‘Reducing the computational complexity of the MCMC algorithm’’ in the appendix.

The comparison of the pore structures obtained from the CLSM samples and from the corresponding fitted models (16) in Figure 15 shows that the model fits the data well. The model fit was assessed quantitatively using the covariance, pore size, and a new measure that characterizes diffusive flux using excursion sets: The goodness of fit using the covariance and

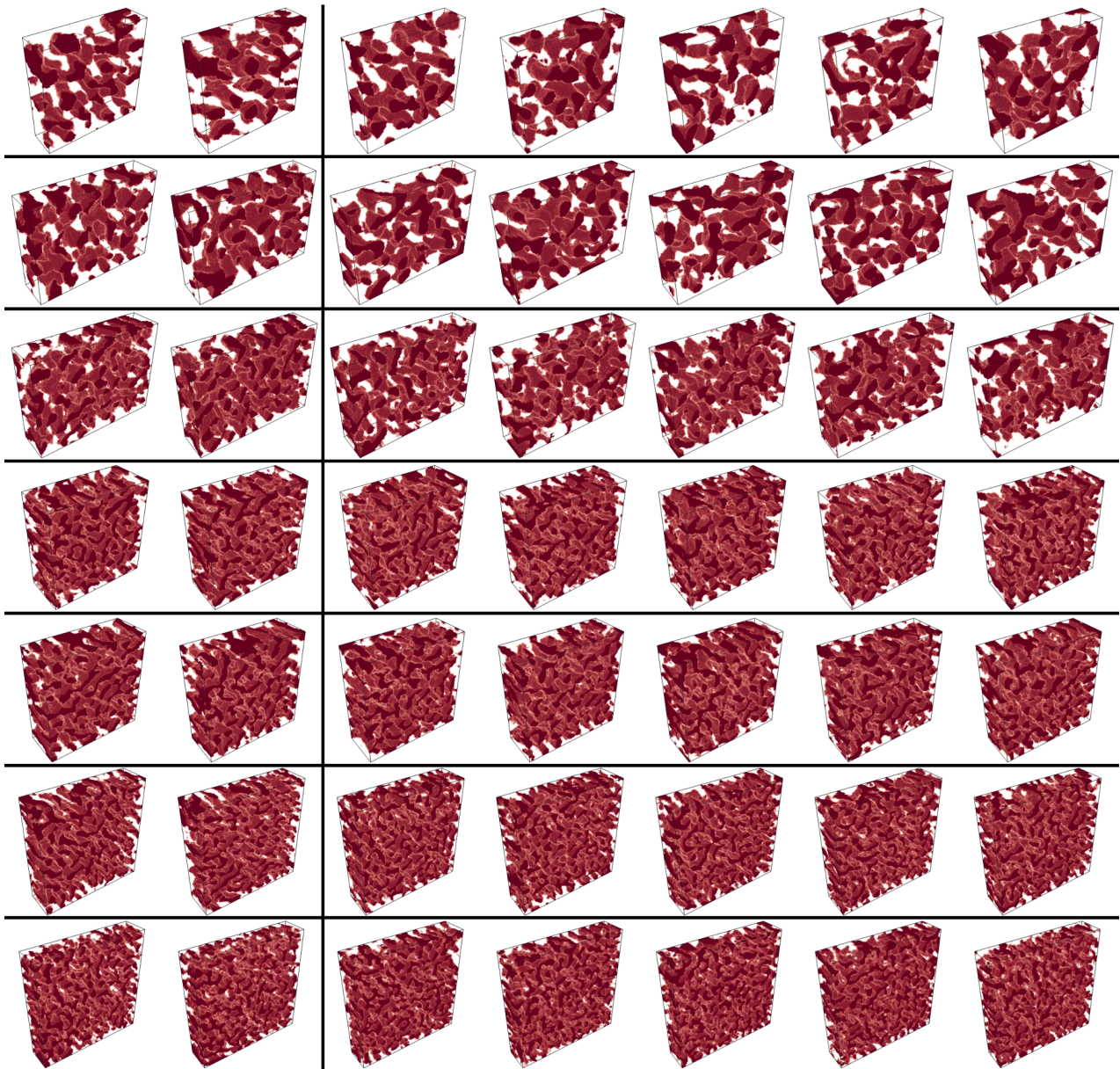


Figure 15: Comparison of microscopy pore structures extracted from the CLSM images of EC/HPC films from Häbel et al. (2017) (left) and five simulations from the corresponding fitted models (right). The microscopy pore structures are shown from front and back. The ordering of the microscopy samples from top to bottom is the same as the ordering of samples  $HPC30_2$ – $HPC40_4$  in Tables 2 and 3 of the appendix of Paper I. Corresponding images for  $HPC30_1$  can be found in Figure 8, Paper I.

pore size were applied to both the binarized CLSM samples corresponding to model (15) and to the filtered data corresponding to the pore model (16), see Figures 9 and 10, Paper I. The diffusive flux and corresponding excursion sets were only computed for the filtered data, see Figure 11, Paper I, as it is not relevant to compute diffusive transport through the noisy CLSM

data.

The goodness of fit using covariance functions were applied to the  $C_t$ - and the  $C_z$ -covariance functions, and not the separable covariance function  $C = C_z C_t$ , thus not checking the validity of using a separable covariance function. However, the goodness of fit of the full model was checked using both the pore size and excursions sets. The goodness of fit of the model was checked using the full covariance  $C$  after the paper was published, and it was concluded that the covariance seemed to fit, although the sample size in the  $z$ -direction may have been too small for a discrepancy in the model fit to be detected.

## 5.2 Paper II

The pore model family from Paper I was used in Paper II to generate pore structures for which multiplicative regression models were fitted relating the pore geometry to diffusive transport computed numerically using Gesualdo, as illustrated in Figure 16. Pore models corresponding to  $4 \times 3 \times 3$  parameter combinations were used of the parameters  $\epsilon$ ,  $\theta_{xy}$  and  $\theta_z$ , with 6 pore structures generated for each pore model. The first pore model parameter was the pore volume fraction  $\epsilon$  of the generated pore structures, and the other two controlled the regularity of the pore geometry in the  $x, y$ -plane and  $z$ -direction, respectively. An additional 30 pore structures were also generated for one of the pore models.

The transport ratio, described in Section 4.1, was introduced in Paper II and multiplicative regression models were fitted with the transport ratio  $TR$  as response variable and pore geometry measures, described in Section 4.3, as predictors. I.e. multiplicative regression models of the form

$$TR = \alpha Pred_1^{\beta_1} \dots Pred_n^{\beta_n}, \quad (17)$$

were fitted, with model parameters  $\alpha, \beta_1, \dots, \beta_n$ , and predictors  $Pred_1, \dots, Pred_n$ . Note the difference compared to the model (13) presented above. The model (13) could be seen as being more accurate, since the predicted values of  $TR$  are guaranteed to take values in the unit interval  $[0, 1]$  in that model. If the model (13) is considered the true model, there are probably several important predictors missing in the regression models fitted in Paper II, e.g. predictors capturing the effect of bottlenecks caused by many paths converging in the same pore (see Figure 11) and predictors capturing the effect of dead-end pores. The intercept  $\alpha$  can be seen as a way of adjusting for these missing predictors. The predictors were also not restricted to take values in the unit interval. The predictors could easily be modified to comply with this restriction though, as shown in Paper V.

The regression model (17) was applied at the pore model level, i.e.  $TR$  was the mean of the transport ratios and the predictors were the mean of the respective predictor computed for the 6 pore structures generated from the particular pore model. The regression model was also applied at the pore structure level for the pore model with 36 generated pore structures.

These regression models were constructed similarly to the multiplicative regression models from Stenzel et al. (2016), in which the pore volume fraction, a tortuosity factor and the constrictivity were included as predictors. Some differences with the work presented in Stenzel et al. (2016) were the following:

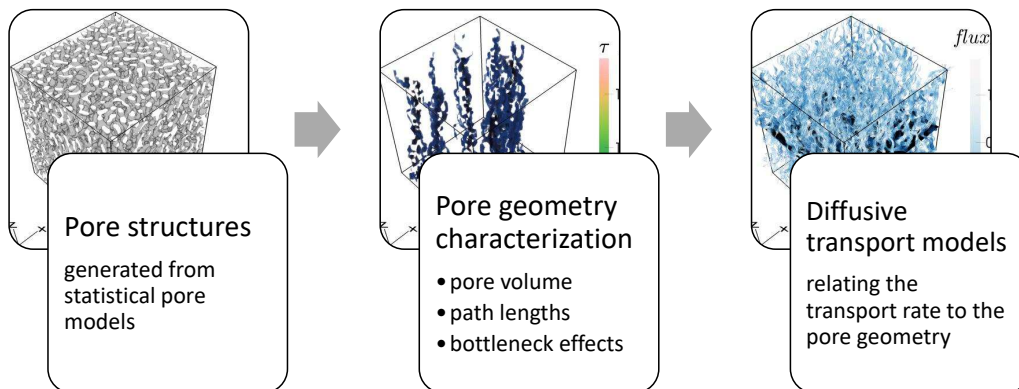


Figure 16: Illustration of the virtual experimental setup used in Papers II and V.

- *More predictors were used*, specifically the fraction connected pores  $\epsilon_C$ , the mean of the local pore size (PS) and the MIP-pore size (MIP) and the standard deviation of the pore size ( $\sigma_{PS}$ ), the MIP-pore size ( $\sigma_{MIP}$ ) and the tortuosity ( $\sigma_\tau$ ).
- *The tortuosity factor was defined to provide exact results for tortuous pores*. The tortuosity factor  $\tau$  was defined in such a way that the equality  $TR = 1/\tau^2$  holds for simple pore structures consisting of separate tubes, i.e. tortuous pores with constant pore size, which includes the pore structures for which the model (11) applies. The tortuosity factor  $\tau$  defined in this way was computed using point-wise tortuosities  $\tau(p)$  for all points  $p$  in the pore space. The tortuosity factor used in Stenzel et al. (2016) on the other hand, denoted  $\tau_{inlet}$ , was computed using point-wise tortuosities  $\tau(p)$  for points  $p$  at the inlet.
- *The regression models were fitted using stepwise regression on the logarithm*. The stepwise regression resulted in regression models with a reduced number of predictors.

For the regression models fitted on the pore model level, the tortuosity factor  $\tau$  was always chosen as a predictor over  $\tau_{inlet}$  by the stepwise regression. The tortuosity factor  $\tau$  also explained a large part, 97%, of the variation in transport rates. Because the regression model with only  $\tau$  as a predictor performed so well, only small increases in model fit were obtained when adding other predictors to the regression model (Table 2, Paper II). However, when the exponent of  $\tau$  was fixed to the theoretically motivated value 2 (see model (11) and (12) above, and section ‘‘Average of the reciprocal of the pointwise geodesic tortuosity’’ of Paper II), regression models which included some of the new predictors, specifically the standard deviation-predictors, explained around twice as much of the variation compared to the regression model which only included the constrictivity used in Stenzel et al. (2016) as a predictor (Table 3, Paper II). A more detailed discussion of the effects of fixing the exponent of  $\tau$  can be found in Section 5.5.

Decreasing the pore volume fraction decreased the transport ratio  $TR$  for all pore models (Figure 5, Paper II). With the interpretation given for  $TR$  in the paper (see Section 4.1), this means that the transport was reduced more compared to an optimal pore structure of the same

pore volume fraction  $\epsilon$ , for lower values of  $\epsilon$ . The diffusive transport also seemed to change in character when the pore volume was decreased: there was a higher proportion of relative (normalized) flux close to zero, i.e. there was a higher proportion pores that did not contribute much to the transport, for lower values of  $\epsilon$  (Figure 6, Paper II). For a thresholded Gaussian field-model such as the one used in this paper, when the threshold is increased, i.e. when  $\epsilon$  is decreased, some of the connections in the resulting pore network are severed. This should lead to a higher prevalence of dead-ends and stronger bottleneck effects caused by many paths converging in the same pore (simply referred to as bottlenecks in Paper II), which could explain the higher proportion pores not contributing to the transport. Judging by the constrictivity (Figure 5(b), appendix of Paper II), bottleneck effects caused by variations in pore size were also stronger for lower  $\epsilon$ .

Regression models using the tortuosity factors  $\tau$  and  $\tau_{\text{inlet}}$  as predictors were fitted to the dataset with 36 pore structures. The regression model with  $\tau$  as a predictor explained 67% of the variation in  $TR$ , whereas the regression model with  $\tau_{\text{inlet}}$  only explained 5% (Figure 8, Paper II). This difference could be explained by the fact that the point-wise tortuosity  $\tau(p)$  was on average higher for points  $p$  further away from the inlet and outlet (Figure 11(b), Paper II). I.e.  $\tau$  captures to a greater extent the effect of pores that are not well-connected to the inlet and outlet, i.e. pores for which  $\tau(p)$  is large, compared to  $\tau_{\text{inlet}}$ .

The dataset with 36 pore structures was also used to quantify boundary effects. An approach to reduce errors by choosing sub-windows with the voxels close to the  $x, y$ -boundary removed was implemented. Here the number of voxels being removed was based on the mean squared error of computed pore geometry characterization measures and diffusion. It was concluded that around 20% of the total number of voxels should be removed for this dataset.

### 5.3 Paper III

The pore geometry characterization methods from Paper II were in Paper III developed further, and were used to characterize three sets of FIB-SEM images of leached films of the EC/HPC coating material. The same dataset was also used in Paper IV. A detailed description of the method used to obtain these FIB-SEM images can be found in Fager et al. (2020), but the method is also described in more detail in Paper IV. A short description of the segmentation algorithm used to obtain the pore geometry of the films can be found in both Paper III and IV.

As noted in Markl et al. (2018), often only simple pore geometry properties such as the pore volume fraction are reported in pharmaceutical applications. Paper III in contrast contains a detailed analysis of the pore shape and connectivity properties of the leached films. The three films originally contained 22%, 30% and 45% HPC, respectively, and were referred to as HPC22, HPC30 and HPC45. The preparation of the EC/HPC films, the FIB-SEM procedure and the binarization algorithm are explained in detail in Paper IV.

A new method for characterizing bottlenecks caused by many paths coinciding in the same pore, such as illustrated in Figure 11, was presented in Paper III. The new measure, termed the geodesic channel-strength, was defined as follows:

**Definition.** Let  $G = \{\text{GeoPath}_{\text{dir}}(p), p \in S\}$  be a set of geodesic paths computed in the direction  $\text{dir} = x, y$ , or  $z$ , corresponding to points  $p \in S$  which are well-distributed throughout

the pore space  $P$ . The geodesic channel-strength  $GeoChannel(p')$  in a point  $p' \in P$  is then given by the proportion paths in  $G$  which pass through  $p'$ .

The geodesic channel-strength can be used to identify main channels, which are defined as parts of the pore space with a high geodesic channel-strength. The main channels can be seen as a simplification of the porous network, which can help to visually identify important features of the network, see Figures 1 and 11, Paper III. Channels of relatively high strength, and high variation in channel-strength between different parts of a pore structure, indicate a bottleneck effect. However, alternative path-ways close to a channel of high strength, and the pore size of the high strength channels should be taken into account when determining if there is a bottleneck effect.

The geodesic channel-strength was implemented as a way of capturing the poor connectivity in the transport direction ( $y$ -direction) in HPC22, and were applied in the transport direction for all three films. The other methods implemented in Paper II for measuring the connectivity (the geodesic distance and geodesic tortuosity) and bottleneck effects (the constrictivity) were also applied. In addition, the pore size with respect to spheres, ellipses and lines were computed, as was a measure of the local variation in pore volume fraction, and a new method for quantifying pore shape, computed by relating maxima of the ellipse- and line-size to the sphere-size was applied.

The pore size measures showed that pores in all three films were relatively flat (Table 2, Paper III), with a strong anisotropy in shape, as the line-sizes were in general shorter in the  $y$ -direction compared to in the other directions (Figure 6, Paper III). There was also an anisotropy in path lengths, as the tortuosity in the  $x$ -direction was considerably lower compared to the tortuosity in the  $y$ -direction (Figures 9 and 10, Paper III). These anisotropy effects could be explained by the process that was used to create the EC/HPC films, in which layers in the  $x, z$ -plane were sprayed consecutively onto a rotating drum, creating a different structure in the  $y$ -direction. The same type of process was used to create the films from Paper I (Häbel et al., 2017), which therefore also explains the anisotropy identified in that paper<sup>5</sup>.

The anisotropy trends were the same for all three films, but were stronger for lower pore volume fractions (lower weight percentage of HPC). Similarly, the tortuosity and the maximum geodesic channel-strength were higher for lower pore volume fractions, but were considerably higher for HPC22 compared to the other two films (Figures 9–12, Paper III). The channel-strength was used to identify a limiting layer in HPC22, in which there were only two channels of relatively high strength that connected the top and bottom of the layer (Figure 11, Paper III). The two main channels in the limiting layer were in fact the only two paths connecting the top and bottom of the limiting layer. As the pore size of the two main channels were relatively small compared to the proportion of paths passing through, it can be concluded that there is a bottleneck effect in this layer. Bottlenecks such as these, which are not caused by variations in pore size, are not captured by the existing methods found in Berg (2012) and Holzer et al. (2013b). The low connectivity in HPC22 with these bottleneck effects could be explained by 22% HPC being at the percolation onset for the coating material, i.e. it is around 22% HPC that

---

<sup>5</sup>Note that the  $z$ -direction is used to denote the direction of transport through the coating material in Paper I and Paper II, and through the pore structures generated from the pore models of Paper V, but the  $y$ -direction is used to denote the direction of transport in Paper III and Paper IV.

the HPC starts to form a fully connected component (Marucci et al., 2009). In conclusion, it was found that the geodesic channel-strength provided insights into the connectivity properties which complemented the information attained from the related geodesic distance- and geodesic tortuosity-measures. In particular, the two bottlenecks identified in the limiting layer of HPC22 were not easily identified using the other two geodesic measures.

A “video” of the geodesic distance computed to the top in the  $y$ -direction of HPC22, which illustrate further the effect of the limiting layer, is found in Figure 13, Paper III. Here seven images of the geodesic distance thresholded at different levels are shown. These images illustrate the need to visually explore the results of the pore geometry characterization to fully understand the connectivity properties of the material. A full video with a gradually increasing threshold can be found in the appendix of Paper III. The video can also be downloaded from [this link](#)<sup>6</sup>.

## 5.4 Paper IV

The dataset from Paper III was in Paper IV studied from a slightly different perspective. The focus in Paper IV was on the structure of paths through the pore structure obtained from the three films, in particular geodesic paths starting at a chosen inlet pore, and the corresponding geodesic channel-strength. This is in contrast to the characterization measures based on geodesic paths presented in Paper III, which were computed from geodesic paths starting at the inlet defined as all pores in the top slice of the pore structure (compare Figure 1, Paper III with Figures 2 and 3, Paper IV).

A method for visualizing the interconnectivity of the pore structure of the three films was developed, where geodesic paths were divided into groups by length. 40 geodesic paths were chosen randomly from three groups containing short, intermediate and long geodesic paths, respectively, for each film. The three groups contained all geodesic paths with tortuosities lower than the 20% tortuosity-quantile (short paths); all geodesic paths with tortuosities between the 40% and 60% tortuosity-quantile (intermediate paths); and all geodesic paths with tortuosities higher than the 80% tortuosity-quantile (long paths). The 40 geodesic paths from the same group and the same film were combined in one figure, creating a  $3 \times 3$  table of figures (Figure 8, Paper IV), which shows that there was a substantial difference in path structure for geodesic paths through HPC22 compared to geodesic paths through the other two films. Paths through HPC22 were much more winded, whereas paths through HPC30 and HPC40 were relatively straight and short. Visualizing sets of geodesic paths in this way helps give an understanding of the variability in path structure. The visualization quickly gets unintelligible as the number of paths in the set is increased though. Choosing a specific inlet pore and dividing paths into groups by lengths, as was done in Paper IV, helped to keep the visualizations interpretable.

The geodesic channel-strength, which in Paper III was computed from a large set of geodesic paths starting at the chosen inlet pore, quantified the trends observed in the visualization of geodesic paths. A limiting layer with only two main channels was observed in HPC22, which just as in Paper III were concluded to be bottlenecks as these were the only two pores connecting the top to the bottom of the pore structure. This demonstrates how the geodesic channel-strength can be used as a method for visually identifying the central features of the porous network

---

<sup>6</sup><https://chalmersuniversity.box.com/s/jew08700m49a77hetyncrdrz7bq5vn5b>

by visualizing only “highly travelled” parts of the porous network. The limiting layer e.g. is difficult to detect from visual inspection of e.g. all pores that are connected to both the top and bottom of the pore structure, as there are more connected pores in the limiting layer than just the two bottlenecks (see the video in the appendix of Paper III). These pores are however not visible in the visualization of the geodesic channel-strength, as very few paths pass through them.

## 5.5 Paper V

In Paper V, the new geodesic channel measure, invented in Paper III, was developed further. Two aspects which need to be taken into account when determining if a pore with high channel-strength is a bottleneck are (1) the size of the pore and (2) whether or not there are alternative pathways, slightly longer than the path through the pore with high channel-strength, that can take some of the pressure of the high channel-strength pore. Two new measures were introduced in Paper V which address these two aspects. The first, termed the pore size-channels-measure, relates the size of pores with high channel-strength to the maximum pore size observed in the pore structure. The second, termed the closed pore-tortuosity, measures the increase in tortuosity when a pore with high channel-strength is “closed of”, i.e. when a subset of the pore is removed so that no paths can pass through it. A slightly different version of the geodesic channel-strength was used in Paper V, for computational efficiency.

Multiplicative regression models of the form (17) used in Paper II were fitted with predictors based on the geodesic channel strength, the two new measures, the tortuosity factor  $\tau$  defined in Paper II, the constrictivity, and two of the measures based on standard deviations of tortuosity and pore size, respectively, found to be good predictors in Paper II. The predictors were in Paper V restricted to take values in the unit interval. The arguments from Paper II for the model (11), which in Paper II was used to motivate the new definition of the tortuosity factor, was in Paper V used to motivate *the core model*

$$TR = \frac{P}{\tau^2}. \quad (18)$$

Here  $P$  is a compounded factor which is restricted to take the value 1 for simple pore structures for which the model (11) is valid. General multiplicative regression models where the exponent of  $\tau$  was included as a model parameter were compared with multiplicative regression models with the exponent of  $\tau$  fixed to 2 to fit with the core model, as was also done in Paper II.

A reference-dataset, with pore structures consisting of tortuous tubes, was created to confirm the validity of the core model. Two datasets created from relatively simple random network-models, referred to as the Bottleneck 1- and Bottleneck 2-datasets, consisted of pore structures with a wide variation in the bottleneck effect caused by many paths converging in the same pore. Another dataset, termed the Polymer film-dataset, consisted of pore structures generated from the pore model fitted in Paper I.

Multiplicative regression models were fitted either with one predictor or two predictors, for all combinations of predictors, and either with  $\tau$  added as a predictor with a free exponent or with  $\tau$  added as a predictor with a fixed exponent. The general regression models with a free exponent of  $\tau$  were referred to as the *one predictor, free exponent-* and the *two predictors, free*

*exponent*-models (results given in Tables 3 and 5, Paper V). The regression models designed to fit with the core model, i.e. models with the exponent of  $\tau$  fixed to 2, were referred to as the *one predictor, core-* and *two predictor, core-*models (results given in Tables 2 and 4, Paper V). To get a better picture of the effect of fixing the exponent of  $\tau$ , the exponent was not only fixed to the theoretical value 2 but to values in an interval  $[2, k_{\max}]$ , where  $k_{\max}$  was chosen large enough so that the optimal exponent in the *one predictor, free exponent*-model was included in the interval (Figure 5, Paper V).

The core model with  $P = 1$  provided a good fit to the reference set as expected, see Figure 4(b), Paper V. Interestingly, it was found that a simple multiplicative regression model with only  $\tau$  as predictor could explain a large part of the variation in transport ratios when fitting the regression to each dataset separately (Figure 4(b), Paper V). The fitted exponent of  $\tau$  could in the Figure be seen to be different for each dataset and to deviate significantly from the theoretical value 2. This effect can be explained by a strong correlation between the tortuosity and e.g. bottleneck effects caused by many paths converging in the same pore, causing overfitting of the regression model with only the tortuosity as predictor. These arguments can be illustrated using the relative diffusive flux shown in three pore structures in Figure 2, Paper V. The pore structure in the top right has less efficient transport ( $TR = 0.24$ ) compared to the other two pore structures ( $TR = 0.57$  and  $TR = 0.55$ ). The top right pore structure also has both a stronger bottleneck and higher tortuosity compared to the other two pore structures, illustrating the strong correlation between the two pore geometry features. Comparing the transport ratio of the pore structure in the top right with the transport ratio of a pore structure with the same pore volume and the same tortuosity, which according to model (11) would be  $TR = 1/\tau^2 = 0.60$ , it is also clear that the tortuosity alone does not explain the transport ratio of the top right pore structure.

Only small improvements in model fit were observed when adding more predictors to the multiplicative regression models, compared to when only using the tortuosity as predictor (free exponent-models). When fixing the exponent of the tortuosity to its theoretical value 2 however (core-models), considerable improvements were observed, especially for the predictors based on quantiles of the geodesic channel strength. The plots of the coefficient of variation for different predictors and different values of the fixed exponent (Figure 5, Paper V) show that the general regression model is unidentifiable, due to the strong correlation between the geodesic channel strength and tortuosity. When taking the arguments for the core model into account, it was concluded that regression models of the form of the core model with the geodesic channel measure added as predictor was the best model.

## 6 MIST, a program package for visualization and characterization of 3-D geometries

The software MIST (Barman et al., 2019) was created as part of the project “Material structures seen through microscopes and spatial statistic”, funded by the Swedish Foundation for Strategic Research, SSF, of which this thesis is a part. Screenshots showing the user interface can be seen in Figure 17. The software is freely available under the CC-BY licence, and was designed to in-

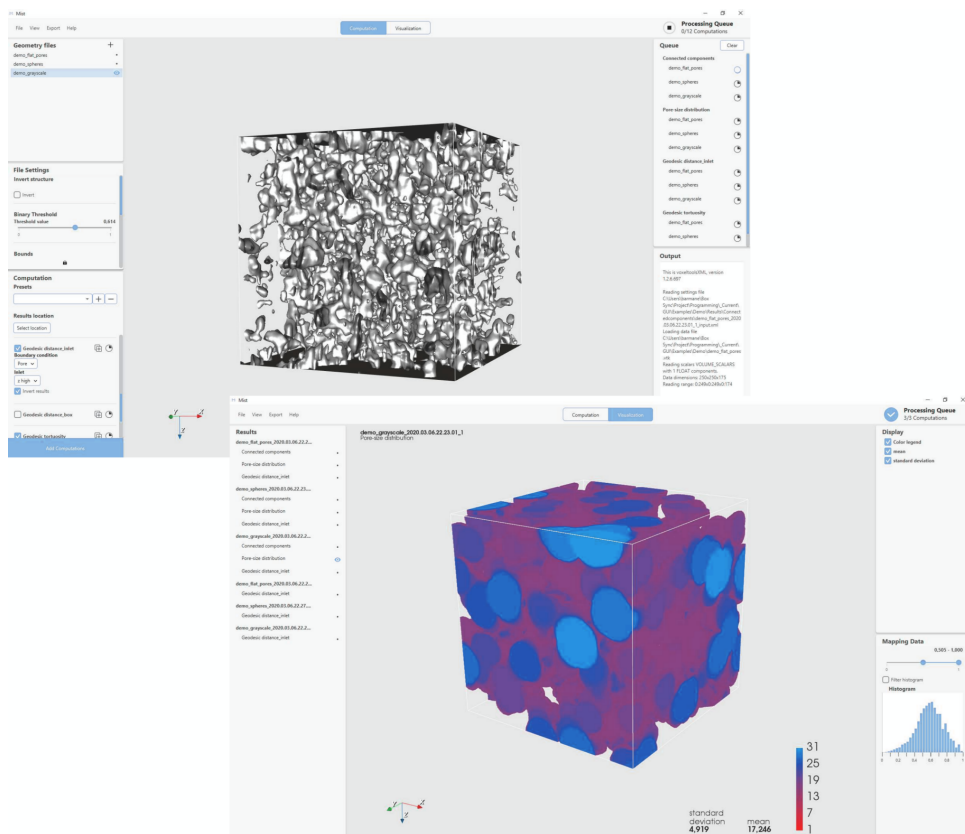


Figure 17: Screenshots of MIST, showing the computation (top) and visualization (bottom) interfaces of the software.

crease the availability of the characterization methods implemented and developed in this thesis (geodesic paths and channel-strengths will soon be included in the characterization methods provided in MIST). The software includes methods to visually explore the pore geometry using the results of the characterization methods, similar to the visualization in the video included in the appendix of Paper III (see link in Section 5.3 above).

[Here is a link<sup>7</sup>](https://chalmersuniversity.box.com/s/37hlfkxvt61tfucob76zysblcrrshppn) from which the software and a document with videos showing how to use the software can be downloaded. The example pore structures shown in the instruction videos can also be downloaded using the link.

---

<sup>7</sup><https://chalmersuniversity.box.com/s/37hlfkxvt61tfucob76zysblcrrshppn>

## References

- P.M. Adler. *Porous Media: Geometry and Transport*. Butterworth-Heinemann, Stoneham, 1992.
- P.M. Adler, C.G. Jacquin, and J.A. Quiblier. Flow in simulated porous media. *International Journal of Multiphase Flow*, 16(4), 1990.
- R.J. Adler. On excursion sets, tube formulas and maxima of random fields. *The Annals of Applied Probability*, 10(1):1–74, 2000.
- R.J. Adler, J.E. Taylor, and K.J. Worsley. *Applications of Random Fields and Geometry, Foundations and Case Studies*. 2013. Manuscript.
- H. Andersson, J. Hjärtsam, M. Stadig, C. von Corswant, and A. Larsson. Effects of molecular weight on permeability and microstructure of mixed ethyl-hydroxypropyl-cellulose films. *European Journal of Pharmaceutical Sciences*, 48(1):240–248, 2013.
- L.M. Anovitz and D.R. Cole. Characterization and analysis of porosity and pore structures. *Reviews in Mineralogy and Geochemistry*, 80(1):61–164, 2015.
- S. Barman, D. Bolin, C. Fager, T. Gebäck, N. Lorén, E. Olsson, H. Rootzén, and A. Särkkä. *MIST – A program package for visualization and characterization of 3D geometries*. 2019.
- G.E. Bell and J. Crank. Influence of imbedded particles on steady-state diffusion. *Journal of the Chemical Society, Faraday Transactions 2: Molecular and Chemical Physics*, 70:1259–1273, 1974.
- C.F. Berg. Re-examining Archie’s law: Conductance description by tortuosity and constriction. *Physical Review E: Statistical, Nonlinear, and Soft Matter Physics*, 86(4):046314, 2012.
- M.J. Blunt, M.D. Jackson, M. Piri, and P.H. Valvatne. Detailed physics, predictive capabilities and macroscopic consequences for pore-network models of multiphase flow. *Advances in Water Resources*, 25(8):1069–1089, 2002.
- M.J. Blunt, B. Bijeljic, H. Dong, O. Gharbi, S. Iglauer, P. Mostaghimi, and A. Paluszny. Pore-scale imaging and modelling. *Advances in Water Resources*, 51:197–216, 2013.
- D. Bolin. Spatial Matérn fields driven by non-Gaussian noise. *Scandinavian Journal of Statistics*, 41(3):557–579, 2014.

- D. Bolin and F. Lindgren. Spatial models generated by nested stochastic partial differential equations, with an application to global ozone mapping. *The Annals of Applied Statistics*, 5(1):523–550, 2011.
- R. Brémond, D. Jeulin, P. Gateau, J. Jarrin, and G. Serpe. Estimation of the transport properties of polymer composites by geodesic propagation. *Journal of Microscopy*, 176(2):167–177, 1994.
- S. Brooks, A. Gelman, G. Jones, and X.L. Meng, editors. *Handbook of Markov Chain Monte Carlo*. CRC press, Boca Raton, 2011.
- P.E. Buis and W.R. Dyksen. Efficient vector and parallel manipulation of tensor products. *ACM Transactions on Mathematical Software (TOMS)*, 22(1), 1996.
- J. Chaniot, M. Moreaud, L. Sorbier, T. Fournel, and J.-M. Becker. Tortuosimetric operator for complex porous media characterization. *Image Analysis and Stereology*, 38:25–41, 2019.
- J.P. Chilès and P. Delfiner. *Geostatistics: Modeling Spatial Uncertainty*. John Wiley & Sons, 2 edition, 2012.
- S.N. Chiu, D. Stoyan, W.S. Kendall, and J. Mecke. *Stochastic Geometry and Its Applications*. John Wiley & sons, Chichester, 3 edition, 2013.
- O.F. Christensen, G.O. Roberts, and M. Sködl. Robust Markov chain Monte Carlo methods for spatial generalized linear mixed models. *Journal of Computational and Graphical Statistics*, 15(1):1–17, 2006.
- N. Cressie and G. Johannesson. Fixed rank kriging for very large spatial data sets. *Journal of the Royal Statistical Society: Series B (Statistical Methodology)*, 70(1):209–226, 2008.
- J.A. Currie. Gaseous diffusion in porous media: II. dry granular materials. *British Journal of Applied Physics*, 11:318–324, 1960.
- J.D. Cutnell and K.W. Johnson. *Physics*. John Wiley & Sons, 2018.
- A.P. Dempster, N.M. Laird, and D.B. Rubin. Maximum likelihood from incomplete data via the EM algorithm. *Journal of the Royal Statistical Society: Series B (Methodological)*, 39:1–38, 1977.
- A. Duda, K. Zbigniew, and M. Maciej. Hydraulic tortuosity in arbitrary porous media flow. *Physical Review E*, 84(3):036319, 2011.
- R. Eymard, T. Gallouët, and R. Herbin. In *Handbook of numerical analysis: VII*, chapter Finite volume methods, pages 713–1018. Elsevier, Amsterdam, 2000.
- C. Fager, M. Röding, A. Olsson, C. von Corswant, N. Lorén, A. Särkkä, and E. Olsson. A review of FIB-SEM tomography of soft poorly conductive materials. *Manuscript submitted to Microscopy and Microanalysis*, 2020.

- L. Fahrmeir and S. Lang. Bayesian inference for generalized additive mixed models based on markov random field priors. *Journal of the Royal Statistical Society: Series C (Applied Statistics)*, 50(2):201–220, 2001.
- R. Foxall and A. Baddeley. Nonparametric measures of association between a spatial point process and a random set, with geological applications. *Journal of the Royal Statistical Society: Series C (Applied Statistics)*, 51(2):165–182, 2002.
- C. Gaetan and X. Guyon. *Spatial Statistics and Modeling*. Springer series in statistics. Springer, New York, 2010.
- G. Gaiselmann, M. Neumann, V. Schmidt, O. Pecho, T. Hocker, and L. Holzer. Quantitative relationships between microstructure and effective transport properties based on virtual materials testing. *AIChE Journal*, 60(6):1983–1999, 2014.
- T. Gebäck and A. Heintz. A lattice Boltzmann method for the advection-diffusion equation with Neumann boundary conditions. *Communications in Computational Physics*, 15(2):487–505, 2014.
- T. Gebäck, M. Marucci, C. Boissier, J. Arnehed, and A. Heintz. Investigation of the effect of the tortuous pore structure on water diffusion through a polymer film using lattice Boltzmann simulations. *The Journal of Physical Chemistry B*, 119(16):5220–5227, 2015.
- A.E. Gelfand, P. Diggle, P. Guttorp, and M. Fuentes, editors. *Handbook of Spatial Statistics*. CRC press, Boca Raton, 2010.
- B. Ghanbarian, A.G. Hunt, R.P. Ewing, and M. Sahimi. Tortuosity in porous media: a critical review. *Soil Science Society of America Journal*, 5:1461–1477, 2013.
- S.J. Harris and P. Lu. Effects of inhomogeneities—nanoscale to mesoscale—on the durability of Li-Ion batteries. *The Journal of Physical Chemistry C*, 117(3):6481–6492, 2013.
- Z. Hashin and S. Shtrikman. A variational approach to the theory of the effective magnetic permeability of multiphase materials. *Journal of Applied Physics*, 33(10):3125–3131, 1962.
- H. Häbel, H. Andersson, A. Olsson, E. Olsson, A. Larsson, and A. Särkkä. Characterization of pore structure of polymer blended films used for controlled drug release. *Journal of Controlled Release*, 222:151–158, 2016.
- H. Häbel, T. Rajala, M. Marucci, C. Boissier, K. Schladitz, C. Redenbach, and A. Särkkä. A three-dimensional anisotropic point process characterization for pharmaceutical coatings. *Spatial Statistics*, 22:306–320, 2017.
- X. He, R.S. Zemel, and M.Á. Carreira-Perpiñán. In *Proceedings of the 2004 IEEE Computer Society Conference on Computer Vision and Pattern Recognition (CVPR'04)*, chapter Multiscale conditional random fields for image labeling. IEEE, 2004.

- D. Heng, P. Tang, J.M. Cairney, H.K. Chan, D.J. Cutler, R. Salama, and J. Yun. Focused-ion-beam milling: a novel approach to probing the interior of particles used for inhalation aerosols. *Pharmaceutical Research*, 24(9):1608–1617, 2007.
- H. Hermann and A. Elsner. Geometric models for isotropic random porous media: A review. *Advances in Materials Science and Engineering*, pages 1–16, 2014.
- R. Hilfer. In K.R. Mecke and D. Stoyan, editors, *Statistical Physics and Spatial Statistics*, chapter Local porosity theory and stochastic reconstruction for porous media, pages 203–241. Springer, Berlin, 2000.
- L. Holzer, B. Iwanschitz, Th. Hocker, L. Keller, O. Pecho, G. Sartoris, Ph. Gasser, and B. Muench. Redox cycling of ni-ysz anodes for solid oxide fuel cells: Influence of tortuosity, constriction and percolation factors on the effective transport properties. *Journal of Power Sources*, 242:179–194, 2013a.
- L. Holzer, D. Weidenmann, B. Münch, L. Keller, M. Prestat, Ph. Gasser, I. Robertson, and B. Grob ty. The influence of constrictivity on the effective transport properties of porous layers in electrolysis and fuel cells. *Journal of Materials Science*, 48(7):2934–2952, 2013b.
- T.J. Hughes, G. Engel, L. Mazzei, and M.G. Larson. In *Discontinuous Galerkin Methods*, chapter A comparison of discontinuous and continuous Galerkin methods based on error estimates, conservation, robustness and efficiency, pages 135–146. Springer, Berlin, 2000.
- J.P. James, H-W. Choi, and J.G. Pharoah. X-ray computed tomography reconstruction and analysis of polymer electrolyte membrane fuel cell porous transport layers. *International Journal of Hydrogen Energy*, 37(23):18216–18230, 2012.
- A.M. Johansen, L. Evers, and N. Whiteley. *Monte Carlo Methods*. Lecture notes. 2007.
- G.L. Jones. On the Markov chain central limit theorem. *Probability Surveys*, 1:299–320, 2004.
- S.H. Kim and H. Pitsch. Reconstruction and effective transport properties of the catalyst layer in PEM fuel cells. *Journal of the Electrochemical Society*, 156(6):B673–B681, 2009.
- A. Lang and J rgen Potthoff. Fast simulation of Gaussian random fields. *Monte Carlo Methods and Applications*, 17(3):195–214, 2011.
- K. Lange. A gradient algorithm locally equivalent to the EM algorithm. *Journal of the Royal Statistical Society: Series B (Methodological)*, 57(2):425–437, 1995.
- S. Larsson and V. Thom e. *Partial Differential Equations with Numerical Methods*. Texts in applied mathematics. Springer, Berlin, 2003.
- R. Law, J. Illian, D.F. Burslem, G. Gratzner, C.V.S. Gunatilleke, and I.A.U.N. Gunatilleke. Ecological information from spatial patterns of plants: insights from point process theory. *Journal of Ecology*, 97(4):606–628, 2009.

- L.P. Lefebvre, J. Banhart, and D.C. Dunand. Porous metals and metallic foams: current status and recent developments. *Advanced engineering materials*, 10(9):775–787, 2008.
- H. Liasneuski, D. Hlushkou, S. Khirevich, A. Höltzel, U. Tallarek, and S. Torquato. Impact of microstructure on the effective diffusivity in random packings of hard spheres. *Journal of Applied Physics*, 116:034904, 2014.
- F. Lindgren, H. Rue, and J. Lindström. An explicit link between Gaussian random fields and Gaussian Markov random fields: the stochastic partial differential equation approach. *Journal of the Royal Statistical Society: Series B (Statistical Methodology)*, 73(4):423–498, 2011.
- W.B. Lindquist, S.-M. Lee, D.A. Coker, K.W. Jones, and P. Spanne. Medial axis analysis of void structure in three-dimensional tomographic images of porous media. *Journal of geophysical research*, 101(B4):8297–8310, 1996.
- K. Malek, M. Eikerling, Q.P. Wang, T.C. Navessin, and Z.S. Liu. Self-organization in catalyst layers of polymer electrolyte fuel cells. *The Journal of Physical Chemistry C*, 161(12):F1254–F1299, 2014.
- D. Markl, A. Strobel, R. Schlossnikl, J. Bötger, P. Bawuah, C. Ridgway, J. Rantanen, T. Rades, P. Gane, K.-E. Peiponen, and J.A. Zeitler. Characterization of pore structures of pharmaceutical tablets: a review. *International Journal of Pharmaceutics*, 538:188–214, 2018.
- M. Marucci, J. Hjærtstam, G. Ragnarsson, F. Iselau, and A. Axelsson. Coated formulations: New insights into the release mechanism and changes in the film properties with a novel release cell. *Journal of Controlled Release*, 136(3):206–212, 2009.
- M. Marucci, J. Arnehed, A. Jarke, H. Matic, M. Nicholas, C. Boissier, and C. von Corswant. Effect of the manufacturing conditions on the structure and permeability of polymer films intended for coating undergoing phase separation. *European Journal of Pharmaceutics and Biopharmaceutics*, 83(2):301–306, 2013.
- G Matheron. *Random sets and integral geometry*. John Wiley & sons, 1975.
- MATLAB. *Version R2017b*. The MathWorks Inc., 2017.
- J.C. Maxwell. *A Treatise on Electricity and Magnetism*, volume 1. Clarendon Press, London, 2 edition, 1881.
- K.R. Mecke and D. Stoyan. *Morphology of condensed matter: Physics and geometry of spatially complex systems*. Springer, 2002.
- A.A. Mohamad. *Lattice Boltzmann Method: Fundamentals and Engineering Applications with Computer Codes*. Springer, London, 2011.

- M.J. Moore. Quantitative analysis of interconnectivity of porous biodegradable scaffolds with micro-computed tomography. *Journal of Biomedical Materials Research Part A*, 71(2):258–267, 2004.
- P.P. Mukherjee and C.Y. Wang. Direct numerical simulation modeling of bilayer cathode catalyst layers in polymer electrolyte fuel cells. *Journal of The Electrochemical Society*, 154(11):B1121–B1131, 2007.
- M. Neumann, J. Staněk, O. Pecho, L. Holzer, V. Beneš, and V. Schmidt. Stochastic 3D modeling of complex three-phase microstructures in SOFC-electrodes with completely connected phases. *Computational Materials Science*, 118:353–364, 2016.
- M. Neumann, C. Hirsch, J. Staněk, V. Beneš, and V. Schmidt. Estimation of geodesic tortuosity and constrictivity in stationary random closed sets. *Scandinavian Journal of Statistics*, 46(3):848–884, 2019.
- J.E. Owen. The resistivity of a fluid-filled porous body. *Journal of Petroleum Technology*, 4(7):169–174, 1952.
- G. Papandreou and A.L. Yuille. Gaussian sampling by local perturbations. In *Advances in Neural Information Processing Systems*, pages 1858–1866. 2010.
- O.M. Pecho, O. Stenzel, B. Iwanschitz, P. Gasser, M. Neumann, V. Schmidt, M. Prestat, T. Hocker, R.J. Flatt, and L. Holzer. 3D microstructure effects in Ni-YSZ anodes: prediction of effective transport properties and optimization of redox stability. *Materials*, 8(9):5554–5585, 2015.
- E.E. Petersen. Diffusion in a pore of varying cross section. *AIChE Journal*, 5:343–345, 1958.
- C. Peyrega and D. Jeulin. Estimation of tortuosity and reconstruction of geodesic paths in 3D. *Image Analysis & Stereology*, 32(1):27–43, 2013.
- A.P. Roberts and M. Teubner. Transport properties of heterogeneous materials derived from gaussian random fields: Bounds and simulation. *Physical Review E: Statistical, Nonlinear, and Soft Matter Physics*, 51(5):4141–4154, 1995.
- H. Rue and L. Held. *Gaussian Markov Random Fields: Theory and Applications*. CRC Press, 2005.
- H. Rue and H. Tjelmeland. Fitting Gaussian Markov random fields to Gaussian fields. *Scandinavian Journal of Statistics*, 29:31–50, 2002.
- H. Rue, S. Martino, and N. Chopin. Approximate Bayesian inference for latent Gaussian models using integrated nested Laplace approximations (with discussion). *Journal of the Royal Statistical Society: Series B (Statistical Methodology)*, 71(2):319–392, 2009.
- M. Schlather. Models for stationary max-stable random fields. *Extremes*, 5(1):33–44, 2002.

- F. Siepmann, J. Siepmann, M. Walther, R.J. MacRae, and R. Bodmeier. Polymer blends for controlled release coating. *Journal of Controlled Release*, 125(1):1–15, 2008.
- J. Siepmann, R.A. Siegel, and M.J. Rathbone, editors. *Fundamentals and Applications of Controlled Drug Delivery*. Springer, New York, 2012.
- O. Stenzel, O. Pecho, L. Holzer, M. Neumann, and V. Schmidt. Predicting effective conductivities based on geometric microstructure characteristics. *AIChE Journal*, 62:1834–1843, 2016.
- O. Stenzel, O. Pecho, L. Holzer, M. Neumann, and V. Schmidt. Big data for microstructure-property relationships: A case study of predicting effective conductivities. *AIChE Journal*, 63(9):4224–4232, 2017.
- R. Thiedmann, C. Hartnig, I. Manke, V. Schmidt, and W. Lehnert. Local structural characteristics of pore space in GDLs of PEM fuel cells based on geometric 3D graphs. *Journal of the Electrochemical Society*, 156(11):B1339–B1347, 2009.
- S. Torquato. Random heterogeneous media: Microstructure and improved bounds on effective properties. *Applied Mechanical Review*, 44(2):37–76, 1991.
- S. Torquato. *Random Heterogeneous Materials: Microstructure and Macroscopic Properties*. Interdisciplinary applied mathematics. Springer, 2002.
- S. Torquato. Optimal design of heterogeneous materials. *Annual Review of Materials Research*, 40:101–129, 2010.
- L. Verde, L. Wang, A.F. Heavens, and M. Kamionkowski. Large-scale structure, the cosmic microwave background and primordial non-gaussianity. *Monthly Notices of the Royal Astronomical Society*, 313(1):141–147, 2000.
- J. Wallin and D. Bolin. Geostatistical modelling using non-Gaussian Matérn fields. *Scandinavian Journal of Statistics*, 42(3):872–890, 2015.
- A.Z. Weber, R.L. Borup, R.M. Darling, P.K. Das, T.J. Dursch, W. Gu, D. Harvey, A. Kusoglu, S. Litster, M.M. Mench, R. Mukundan, J.P. Owejan, J.G. Pharoah, M. Secanell, and I.V. Zenyuka. A critical review of modeling transport phenomena in polymer-electrolyte fuel cells. *Journal of The Electrochemical Society*, 161(2):F1254–F1299, 2014.
- H.L. Weissberg. Effective diffusion coefficient in porous media. *Journal of Applied Physics*, 34(9):2636–2639, 1963.
- P. Whittle. On stationary processes in the plane. *Biometrika*, 41:434–449, 1954.
- P. Whittle. Stochastic processes in several dimensions. *Bulletin of the International Statistical Institute*, 40:974–994, 1963.

- O. Wiener. Die theorie des mischkörpers für das feld der stationären strömung. *Abhandlungen der Mathematisch-Physischen Klasse der Königl. Sächsischen Gesellschaft der Wissenschaften*, 32:509–604, 1912.
- R.J. Wilson and D.J. Nott. Review of recent results on excursion set models. *Image Analysis & Stereology*, 20:71–78, 2001.
- C.L.Y. Yeong and S. Torquato. Reconstructing random media. *Physical Review E: Statistical, Nonlinear, and Soft Matter Physics*, 57(1):495–506, 1998.